

# Do neutrinos become flavor unstable due to collisions with matter in the supernova decoupling region?

Shashank Shalgar<sup>✉</sup> and Irene Tamborra<sup>✉</sup>

*Niels Bohr International Academy and DARK, Niels Bohr Institute, University of Copenhagen, Blegdamsvej 17, 2100 Copenhagen, Denmark*

 (Received 2 August 2023; revised 8 April 2024; accepted 11 April 2024; published 8 May 2024)

In core-collapse supernovae, the neutrino density is so large that neutrino flavor instabilities, leading to flavor conversion, can be triggered by the forward scattering of neutrinos among each other, if a crossing between the angular distributions of electron neutrinos and antineutrinos exists (fast instability in the limit of vanishing vacuum frequency) or in the presence of perturbations induced by the neutrino vacuum frequency (slow instability). Recently, the conjecture has been advanced that neutrino collisions with the medium could be another mean to kick start flavor change (collisional instability). Inspired by a spherically symmetric core-collapse supernova model with mass  $18.6M_{\odot}$ , we compute the neutrino angular distributions solving the kinetic equations for an average energy mode and investigate the occurrence of flavor instabilities at different postbounce times, ranging from the accretion phase to the early cooling phase. We find that fast and slow flavor instabilities largely dominate over the collisional ones in the decoupling region for all postbounce times. While more work is needed to assess the relevance of collisional instabilities in neutrino-dense environments, our findings suggest that neutrino collisions with matter affect the flavor evolution in the decoupling region but are not responsible for triggering flavor conversion, if crossings in the neutrino lepton number angular distribution exist.

DOI: [10.1103/PhysRevD.109.103011](https://doi.org/10.1103/PhysRevD.109.103011)

## I. INTRODUCTION

In dense neutrino astrophysical environments, such as the interior of core-collapse supernovae (SNe) and neutron star mergers, neutrino flavor evolution has a rich phenomenology owing to the nonlinear nature of its evolution [1–5]. The nonlinearity is a consequence of the coherent forward scattering of neutrinos among each other. Flavor conversion is classified as fast, if purely driven by the neutrino-neutrino interaction term for vanishing neutrino vacuum frequency [4,6–10]; in this case, a necessary but not sufficient condition for the development of fast flavor instabilities is the existence of electron lepton number (ELN) crossings in the angular distribution of electron neutrinos and antineutrinos (note that, under the assumption of periodic boundary conditions, the existence of an ELN crossing becomes a sufficient condition for the development of a flavor instability), albeit a large growth rate for such flavor instabilities does not necessarily imply large flavor conversion [11,12]. In addition, neutrino self-interactions could be triggered at high densities by the vacuum frequency in the Hamiltonian [13,14]; in this case, we consider the flavor instability to be slow, since it develops thanks to the vacuum frequency, which is smaller than the neutrino-neutrino interaction strength; note that, in this

case, a system with ELN crossings which is stable for vanishing vacuum frequency may become unstable.

Owing to the nonlinearity of the system, the momentum-changing collisional processes, which are lower-order processes, can have a significant impact on the flavor evolution, despite the widely different characteristic time-scales characterizing flavor evolution and collisions [15–24]. The collisional processes of interest include momentum-changing scattering as well as reactions responsible for the creation and absorption of neutrinos [25–28]. As the neutrino emission properties are affected by the collisional processes, before and during flavor evolution, it is imperative to understand their interplay. First attempts coupling collisions and neutrino flavor evolution self-consistently have been reported in the literature, but there is still a long journey ahead [13,14,29,30].

Existing work employing a given initial ELN angular distribution with a crossing finds that the effect of collisions on flavor evolution is to isotropize the angular distribution, with a resulting enhancement or suppression of flavor conversion according to the initial ELN distributions [15,17,18,31]. On the other hand, a system with no flavor instability in the absence of the collision term can also become unstable in the flavor space because of the so-called collisional instabilities [16,20–22,30–32].

In this paper, we aim to investigate slow,<sup>1</sup> fast, and collisional flavor instabilities, not relying on arbitrary neutrino angular distributions but rather solving the neutrino kinetic equations with the collision terms for an average energy mode to obtain the neutrino angular distributions for each flavor. To this purpose, we rely on static hydrodynamic backgrounds and thermodynamic properties extrapolated at different postbounce snapshots of a spherically symmetric core-collapse SN model with mass  $18.6M_{\odot}$  [33]. To compute the neutrino angular distributions, in the collisional kernel, we include emission and absorption of neutrinos through bremsstrahlung, pair production, and beta reactions. In addition, we consider the direction-changing effects due to neutral current scattering of neutrinos on nucleons. We then investigate through the linear stability analysis whether collisional, slow, or fast flavor instabilities exist.

The manuscript is organized as follows. Section II introduces the neutrino quantum kinetic equations; then we discuss the procedure adopted to obtain the neutrino angular distributions solving the kinetic equations in the absence of flavor conversion in Sec. III. In Sec. IV, we perform the linear stability analysis for the homogeneous mode, with as well as without the collision term in order to understand the effect of collisional instabilities, while we discuss the impact of spatial inhomogeneities in Sec. V. We summarize our findings and offer an outlook in Sec. VI. In addition, Appendix A provides an outline of the collision terms responsible for the production, absorption, and momentum-changing interactions; while a comparison of the neutrino number densities computed in this work with the ones obtained from the hydrodynamical SN simulation is shown in Appendix B.

## II. NEUTRINO QUANTUM KINETIC EQUATIONS

For the sake of simplicity, we consider two monoenergetic neutrino flavors,  $\nu_e$  and  $\nu_x$  with  $x = \mu, \tau$  (or a linear combination of the two). The equations of motion of neutrinos and antineutrinos are, respectively,

$$i\left(\frac{\partial}{\partial t} + \vec{v} \cdot \vec{\nabla}\right)\rho = [H, \rho] + i\mathcal{C}[\rho, \bar{\rho}], \quad (1)$$

$$i\left(\frac{\partial}{\partial t} + \vec{v} \cdot \vec{\nabla}\right)\bar{\rho} = [\bar{H}, \bar{\rho}] + i\bar{\mathcal{C}}[\rho, \bar{\rho}], \quad (2)$$

with  $\rho$  and  $\bar{\rho}$  being  $2 \times 2$  density matrices representing the flavor content of neutrinos and antineutrinos, respectively. The diagonal components of the density matrices ( $\rho_{ii}$ , with

<sup>1</sup>In this work, slow flavor instability indicates a flavor instability that vanishes for zero vacuum frequency, independently on the existence of crossings in the lepton number angular distribution. For fast instabilities, instead, we mean instabilities that arise in the limit of vanishing vacuum frequency.

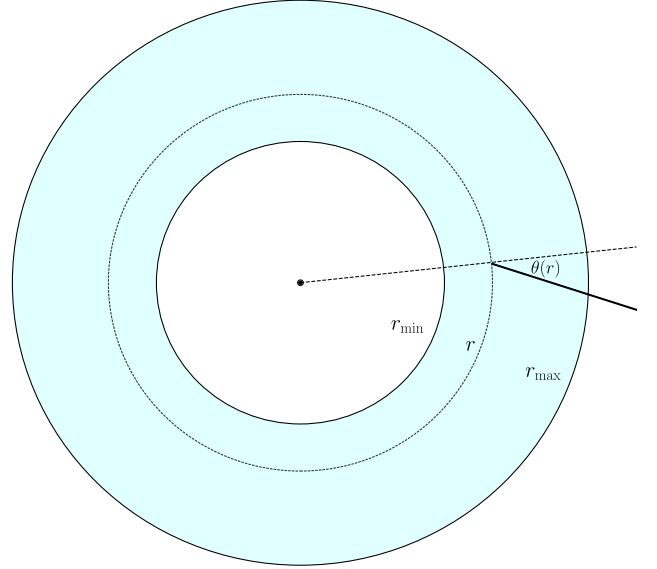


FIG. 1. Schematic diagram of the shell within which we solve the neutrino kinetic equations taking into account emission, absorption, and direction-changing processes. The polar angle  $\theta$  is defined with respect to the radial direction. It should be noted that  $\theta$  changes with the radius for a given trajectory.

$i = e, x$ ) represent the neutrino occupation numbers [in units of  $1/\text{cm}^3$ ]; the number density of a given species,  $n_i$ , at a given location is obtained by  $\int_{-1}^1 \rho_{ii} d \cos \theta$ . In Eqs. (1) and (2), the dependence of the density matrices on the polar angle  $\theta$  (measured with respect to the radial direction; see Fig. 1) and radius  $r$  is suppressed for the sake of brevity.

The velocity vector is represented by  $\vec{v}$ , while  $\vec{\nabla}$  is the gradient operator. The inner product of the two is given by

$$\vec{v} \cdot \vec{\nabla} = \cos \theta \frac{\partial}{\partial r} + \left(\frac{\sin^2 \theta}{r}\right) \frac{\partial}{\partial \cos \theta}, \quad (3)$$

where the dependence on the azimuthal angle  $\phi$  is ignored due to the assumption of spherical symmetry.

The Hamiltonians for neutrinos and antineutrinos ( $H = H_{\text{vac}} + H_{\text{mat}} + H_{\nu\nu}$  and  $\bar{H} = -H_{\text{vac}} + H_{\text{mat}} + H_{\nu\nu}$ , respectively) are made of the vacuum, matter, and the self-interaction terms:

$$H_{\text{vac}} = \frac{\omega_{\text{vac}}}{2} \begin{pmatrix} -\cos 2\theta_{\text{V}} & \sin 2\theta_{\text{V}} \\ \sin 2\theta_{\text{V}} & \cos 2\theta_{\text{V}} \end{pmatrix}, \quad (4)$$

$$H_{\text{mat}} = \begin{pmatrix} \lambda & 0 \\ 0 & 0 \end{pmatrix}, \quad (5)$$

$$H_{\nu\nu} = \sqrt{2}G_{\text{F}} \int d \cos \theta' [\rho(\cos \theta') - \bar{\rho}(\cos \theta')] \times (1 - \cos \theta \cos \theta'). \quad (6)$$

In the vacuum Hamiltonian, the vacuum frequency is  $\omega_{\text{vac}} = \Delta m^2/2\epsilon_\nu$ , with  $\Delta m^2 = 2.5 \times 10^{-3}$  and  $\epsilon_\nu$  being the average neutrino energy calculated over all species, while the mixing angle is  $\theta_V = 10^{-3}$ . In the matter term, the strength of neutrino-matter interactions is given by  $\lambda = \sqrt{2}G_F n_e$ , with the electron number density being  $n_e = Y_e \rho_B/m_N$ , where  $Y_e$  is the electron fraction,  $\rho_B$  is the baryon mass density, and  $m_N$  is the nucleon mass (in the following, we restrict our analysis to the linear regime in which the matter term can be ignored because it does not affect the instability of the system). Note that, when we carry out the linear stability analysis in the following sections, we neglect the matter term and effectively account for it though a smaller value for the mixing angle (i.e.,  $\theta_V = 10^{-3}$ ). The strength of the self-interaction potential, generally denoted by  $\mu = \sqrt{2}G_F n_{\nu_e}$ , characterizes the  $\nu$ - $\nu$  term of the Hamiltonian.

The collision term, schematically represented by the functionals  $\mathcal{C}$  and  $\bar{\mathcal{C}}$ , includes the absorption, emission, and direction-changing processes defined as outlined in Appendix A:

$$\begin{aligned} \mathcal{C}[\rho, \bar{\rho}] &= \mathcal{C}_{\text{emit}} - \mathcal{C}_{\text{absorb}} \odot \rho(\cos \theta) \\ &+ \frac{\mathcal{C}_{\text{dir-ch}}}{2} \int d \cos \theta' [-\rho(\cos \theta) + \rho(\cos \theta')] \\ &+ \cos \theta \mathcal{C}_{\text{ani}} \int d \cos \theta' \cos \theta' \rho(\cos \theta'), \end{aligned} \quad (7)$$

$$\begin{aligned} \bar{\mathcal{C}}[\rho, \bar{\rho}] &= \bar{\mathcal{C}}_{\text{emit}} - \bar{\mathcal{C}}_{\text{absorb}} \odot \bar{\rho}(\cos \theta) \\ &+ \frac{\bar{\mathcal{C}}_{\text{dir-ch}}}{2} \int d \cos \theta' [-\bar{\rho}(\cos \theta) + \bar{\rho}(\cos \theta')] \\ &+ \cos \theta \bar{\mathcal{C}}_{\text{ani}} \int d \cos \theta' \cos \theta' \bar{\rho}(\cos \theta'). \end{aligned} \quad (8)$$

Here,  $\mathcal{C}_{\text{emit}} = \text{diag}(\mathcal{C}_{\text{emit}}^{ee}, \mathcal{C}_{\text{emit}}^{xx})$  and  $\bar{\mathcal{C}}_{\text{emit}} = \text{diag}(\bar{\mathcal{C}}_{\text{emit}}^{ee}, \bar{\mathcal{C}}_{\text{emit}}^{xx})$  govern the emission rate for each neutrino flavor.  $\mathcal{C}_{\text{absorb}}$  and  $\bar{\mathcal{C}}_{\text{absorb}}$  are matrices, and  $\odot$  represents elementwise multiplication:

$$\begin{aligned} \mathcal{C}_{\text{absorb}} \odot \rho(\cos \theta) &= \mathcal{C}_{\text{absorb}}^{ee} \rho_{ee} + \mathcal{C}_{\text{absorb}}^{ex} \rho_{ex} \\ &+ \mathcal{C}_{\text{absorb}}^{xe} \rho_{xe} + \mathcal{C}_{\text{absorb}}^{xx} \rho_{xx}, \\ \bar{\mathcal{C}}_{\text{absorb}} \odot \bar{\rho}(\cos \theta) &= \bar{\mathcal{C}}_{\text{absorb}}^{ee} \bar{\rho}_{ee} + \bar{\mathcal{C}}_{\text{absorb}}^{ex} \bar{\rho}_{ex} \\ &+ \bar{\mathcal{C}}_{\text{absorb}}^{xe} \bar{\rho}_{xe} + \bar{\mathcal{C}}_{\text{absorb}}^{xx} \bar{\rho}_{xx}, \end{aligned} \quad (9)$$

which is linearly proportional to the number of neutrinos at a given location representing the rate at which neutrinos are absorbed by the surrounding matter [34]. The off-diagonal components of  $\mathcal{C}_{\text{absorb}}$  and  $\bar{\mathcal{C}}_{\text{absorb}}$  are the average of the diagonal elements of the diagonal terms. The terms  $\mathcal{C}_{\text{dir-ch}}$  and  $\bar{\mathcal{C}}_{\text{dir-ch}}$  describe the direction-changing neutral current scatterings, which do not change the number of neutrinos

and are flavor independent. The  $\mathcal{C}_{\text{ani}}$  and  $\bar{\mathcal{C}}_{\text{ani}}$  terms depend on the proton and neutron fractions. Moreover, we take into account the anisotropy in the direction-changing scatter term.

In Eqs. (7) and (8), the emission and absorption terms seem to be independent of each other; however, that is not the case and they are related by Kirchoff's law as explained in Appendix A. Hence, given either the absorption or the emission rate, the other can be calculated (for this reason, in Appendix A, we provide only the absorption rates for all the processes).

### III. STEADY STATE NEUTRINO ANGULAR DISTRIBUTIONS

We adopt the outputs of a one-dimensional hydrodynamical simulation of a SN with mass  $18.6M_\odot$ , SFHo nuclear equation of state without muons, and gravitational mass  $1.4M_\odot$  [33]. We consider static hydrodynamical backgrounds and thermodynamical quantities, as well as the local neutrino number density and first energy moment, for selected time snapshots extracted at postbounce times  $t_{\text{pb}} = 0.05, 0.12, 0.25, 0.5, 0.75,$  and  $1$  s, which are representative of the accretion as well as the early Kelvin-Helmholtz cooling phases. Then, we use these quantities as inputs to calculate the collision terms [Eqs. (7) and (8)]. The relevant properties of our benchmark hydrodynamical SN simulations adopted to compute the collision terms are illustrated in Fig. 2 (see also Appendix A).

The neutrino angular distributions are not provided by the hydrodynamic simulation; hence, we compute them solving Eqs. (1) and (2) and imposing  $H = \bar{H} = 0$ . Since we are interested only in the angular distributions in the proximity of the decoupling region, we solve Eqs. (1) and (2) in a radial shell (see Fig. 1) whose width  $[r_{\text{min}}, r_{\text{max}}]$  differs for each postbounce time as summarized in Table I and has been chosen such that the minimum radius  $r_{\text{min}}$  has a number density of neutrinos that coincides with the energy-integrated Fermi-Dirac distribution extracted from the hydrodynamical simulation (i.e., at large optical depth, such that neutrinos are fully coupled with matter), while neutrinos are completely decoupled at the maximum radius  $r_{\text{max}}$  [i.e., the backward component of the neutrino and antineutrino number densities is negligible:  $\rho_{ii}(\cos \theta) \approx 0$  for  $\cos \theta < 0$ ]. We solve the neutrino kinetic equations starting with no neutrinos and antineutrinos in the shell. As the system evolves in time, the simulation shell is populated with neutrinos and antineutrinos with the boundary conditions being guided by the hydrodynamical simulation as explained above.

For each time snapshot, we use a grid with 75 radial bins and 75 angular bins uniformly spread over  $\cos \theta$  and solve the neutrino kinetic equations for the time interval required to achieve a classical steady state configuration.

Figure 3 shows the radial profiles of the angle-integrated neutrino number densities computed for all three flavors

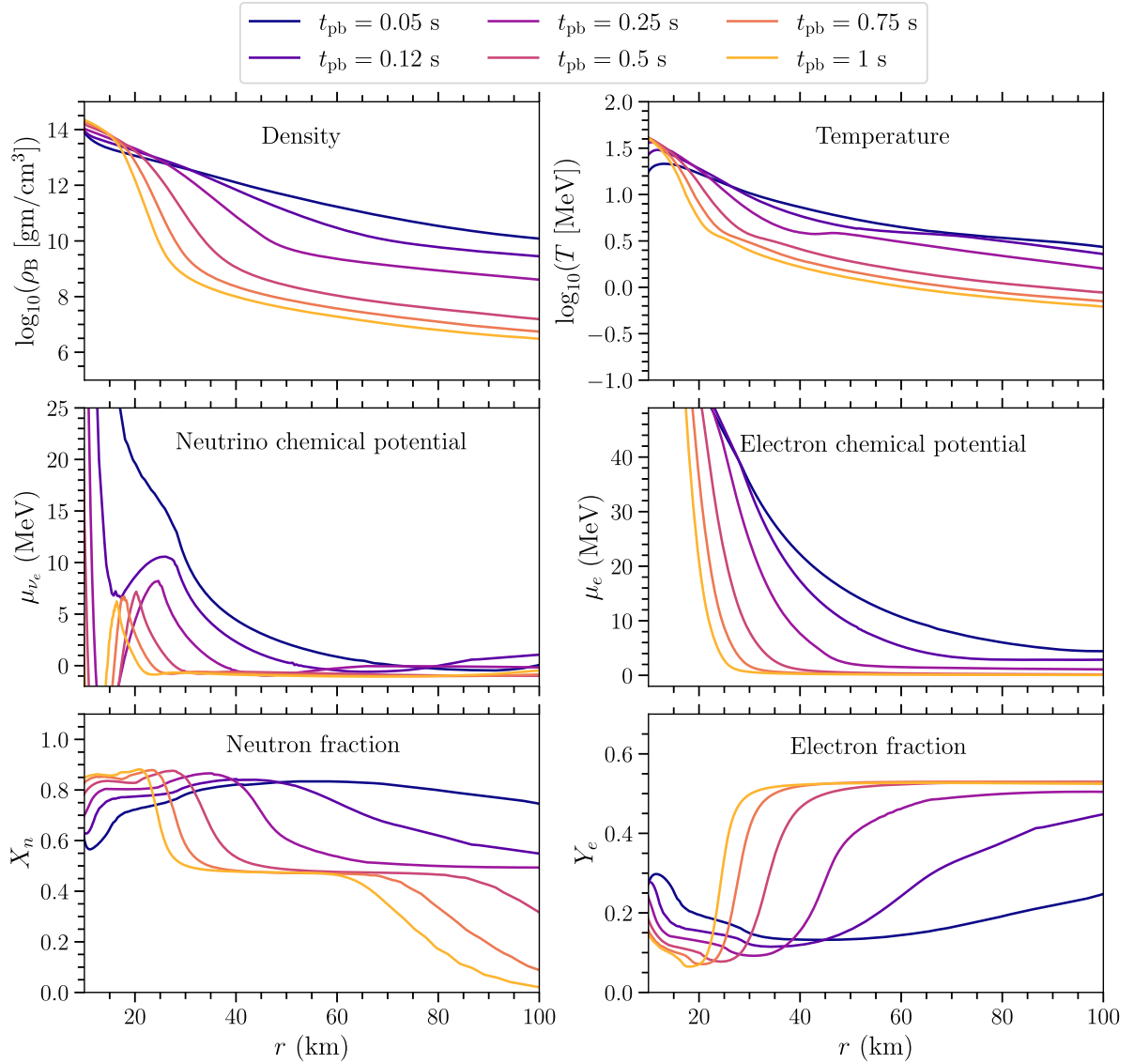


FIG. 2. Radial profiles of the characteristic quantities extracted from our benchmark hydrodynamical SN simulation (see the main text for details) at the postbounce times  $t_{\text{pb}} = 0.05, 0.12, 0.25, 0.5, 0.75,$  and  $1$  s and then adopted to compute the neutrino angular distributions. The different panels represent the baryon number density, the electron temperature, the neutrino and electron chemical potentials, and the neutron and electron fractions, from top left to bottom right, respectively.

TABLE I. Values of  $r_{\text{min}}$  and  $r_{\text{max}}$  used for each postbounce time snapshot to take into account the varying location and width of the decoupling region (see also Fig. 1).

$t_{\text{pb}}$ (s)	$r_{\text{min}}$ (km)	$r_{\text{max}}$ (km)
0.05	25	150
0.12	25	100
0.25	22	57
0.5	20	35
0.75	17	32
1	16	31

through the procedure described above. While involving some approximations, our method allows us to reproduce a local neutrino density in agreement with the output of our benchmark hydrodynamical simulation, as shown in Appendix B. We note that, due to the single-energy approximation used in this paper for simplicity, we slightly overestimate the number density of  $\bar{\nu}_e$  with respect to the one of  $\nu_e$  at large radii when comparing with our benchmark hydrodynamical simulation (see also Fig. 11). As shown later, the fast flavor instability is triggered by the presence of ELN crossings that would be still present, despite the single-energy approximation; hence, the relative importance of fast flavor instabilities with respect to the collisional ones is not affected by the single-energy

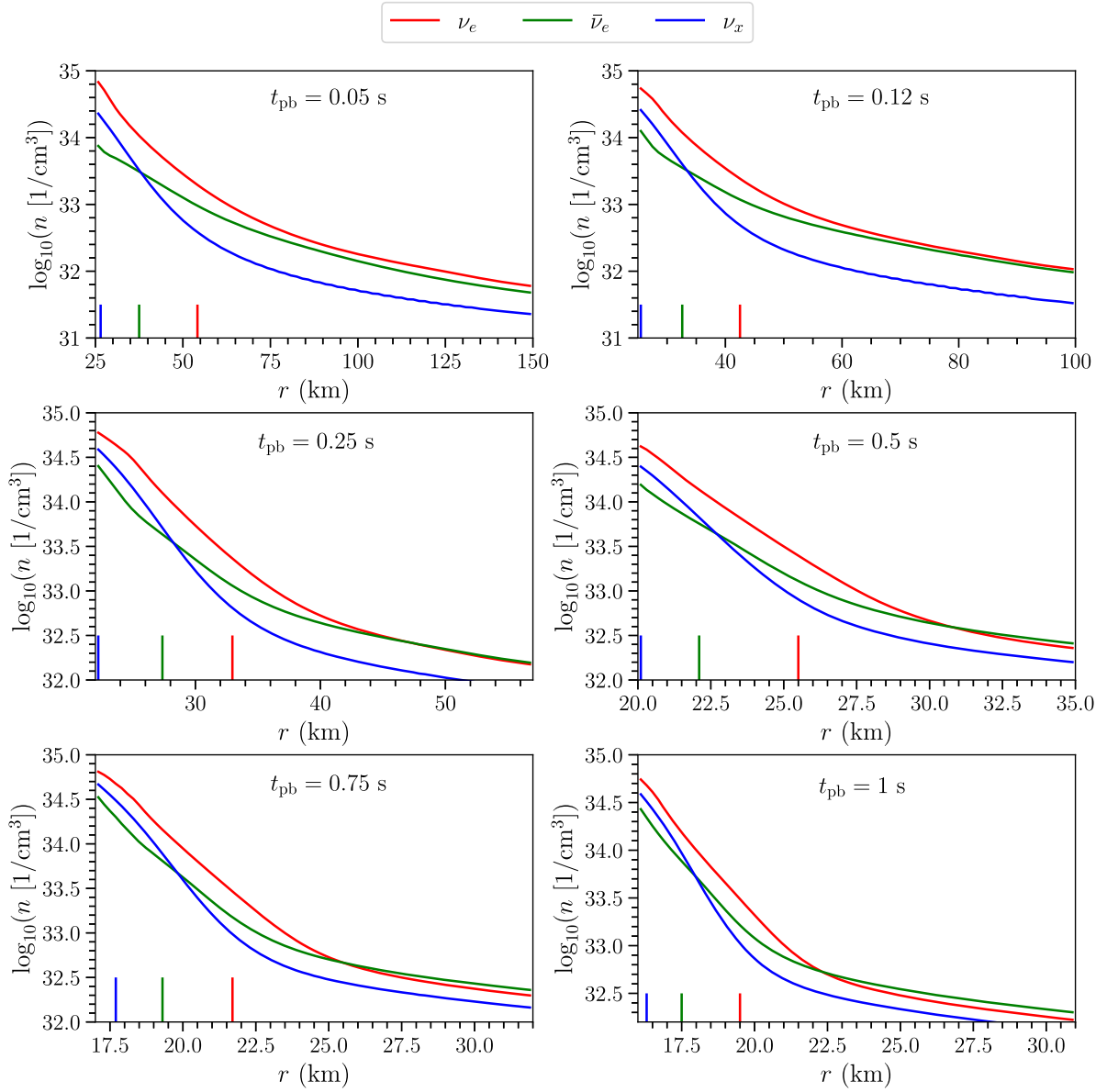


FIG. 3. Radial evolution of the number densities of  $\nu_e$  (in red),  $\bar{\nu}_e$  (in green), and  $\nu_x$  (in blue) for selected postbounce time snapshots and computed solving the neutrino kinetic equations. We mark the radius of neutrino decoupling through a vertical line; this is the radius at which the number density deviates from a Fermi-Dirac distribution (see Appendix B). One can see that the decoupling surface shrinks as a function of time. Note that the radial range is not the same for all time snapshots.

treatment. We stress that the goal of the procedure illustrated in this section is not to reproduce the neutrino properties obtained through the hydrodynamical simulation but rather to obtain neutrino angular distributions that are not arbitrary but inspired by conditions found in the SN interiors.

We define the decoupling radius as the one at which the neutrino number density differs from the Fermi-Dirac one up to 1% (see Appendix B) and mark such radius in Fig. 3 to guide the eye. One can see from Fig. 3 that the decoupling radius becomes smaller as the postbounce time increases. Because of the different nature of their

interactions, while the electron flavors decouple over a broader radial range, the nonelectron flavor decouples almost instantaneously [35].

Figure 4 displays an example of the radial evolution of the neutrino angular distributions computed through the procedure illustrated above for  $t_{\text{pb}} = 0.05$  s. As also found in Ref. [35], the angular distributions become progressively forward peaked as a function of the radial distance and have an angular spread that is the largest for  $\nu_e$ , followed by  $\bar{\nu}_e$  and  $\nu_x$ .

Figure 5 focuses on the radial evolution of the ELN angular distribution for a representative postbounce time

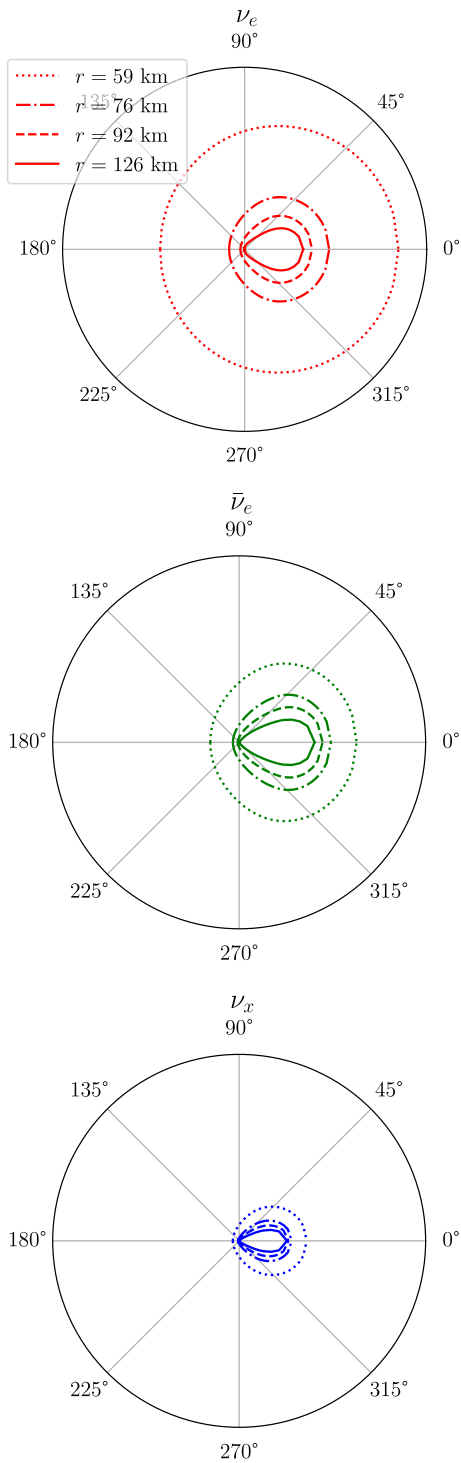


FIG. 4. Polar diagram of the radial variation of the spectral intensity of  $\nu_e$ ,  $\bar{\nu}_e$ , and  $\nu_x$ , from top to bottom, respectively, computed solving the neutrino kinetic equations. The selected radii and the time snapshot  $t_{\text{pb}} = 0.05$  s have been chosen for illustrative purposes. One can see that the neutrino distributions become progressively forward peaked as  $r$  increases, with an angular spread that is largest for  $\nu_e$ , followed by  $\bar{\nu}_e$ , and then  $\nu_x$ .

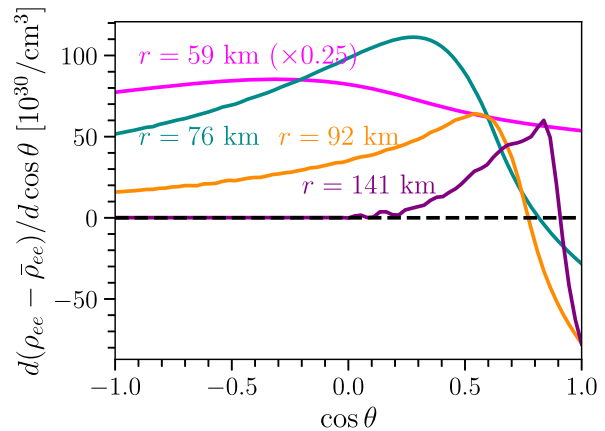


FIG. 5. Angular distribution of the ELN for  $t_{\text{pb}} = 0.05$  s extracted at different radii as indicated. We find ELN crossings for all considered postbounce time snapshots.

snapshot ( $t_{\text{pb}} = 0.05$  s); interestingly, we find ELN crossings for most radii. This finding holds for all postbounce times considered in this work for our benchmark SN model and is in contrast with the results presented in Ref. [35]; the latter concluded, through a systematic analysis of different one-dimensional SN models, that ELN crossings are not present in one-dimensional hydrodynamical simulations, albeit ELN crossings were found in multidimensional SN simulations [36–41]. The results presented in Fig. 5 seem to fulfill the criterion of Ref. [28] that linked the occurrence of ELN crossings to comparable number densities of neutrinos and antineutrino (see also Refs. [22,24]). Yet, the reason why ELN crossings are found in this work but not in Ref. [35] requires further investigation and will be the focus of an upcoming dedicated paper [42]—we stress that the purpose of this work is to rely on the angular distributions derived from first principles to investigate the interplay among fast, slow, and collisional instabilities. The different findings could be connected to the fact that the protoneutron star cooling model of our benchmark SN simulation includes effects from protoneutron star convection (treated by a mixing-length approximation [1,43]) in contrast to the SN models investigated in Ref. [35]. Other reasons might be the different nuclear equation of state (SFHo for our benchmark SN model vs Lattimer and Swesty with compressibility modulus  $K = 220$  MeV in Ref. [35]) or secondary subtle differences in our neutrino transport results compared to those obtained with the VERTEX transport used in Ref. [35].

#### IV. LINEAR STABILITY ANALYSIS FOR THE HOMOGENEOUS MODE

The radial range where significant flavor evolution might develop can be determined through the linear stability analysis [10,44–46]. In this section, we linearize Eqs. (1)

and (2) assuming homogeneity (i.e., ignoring the advective term in the neutrino kinetic equations) and perform the linear stability analysis with and without the collision term to investigate the impact of collisional instabilities. Since we consider monoenergetic neutrinos for simplicity, we here assume that the neutrino energy  $\epsilon_\nu$  entering  $\omega_{\text{vac}}$

changes as a function of the radius and it coincides with the average of the first energy moments extracted from the hydrodynamical SN simulation over all four flavors (see the bottom right panel in Fig. 9).

The linearized version of Eqs. (1) and (2) for the off-diagonal terms of the density matrices at a given  $r$  and  $\cos \theta$  is

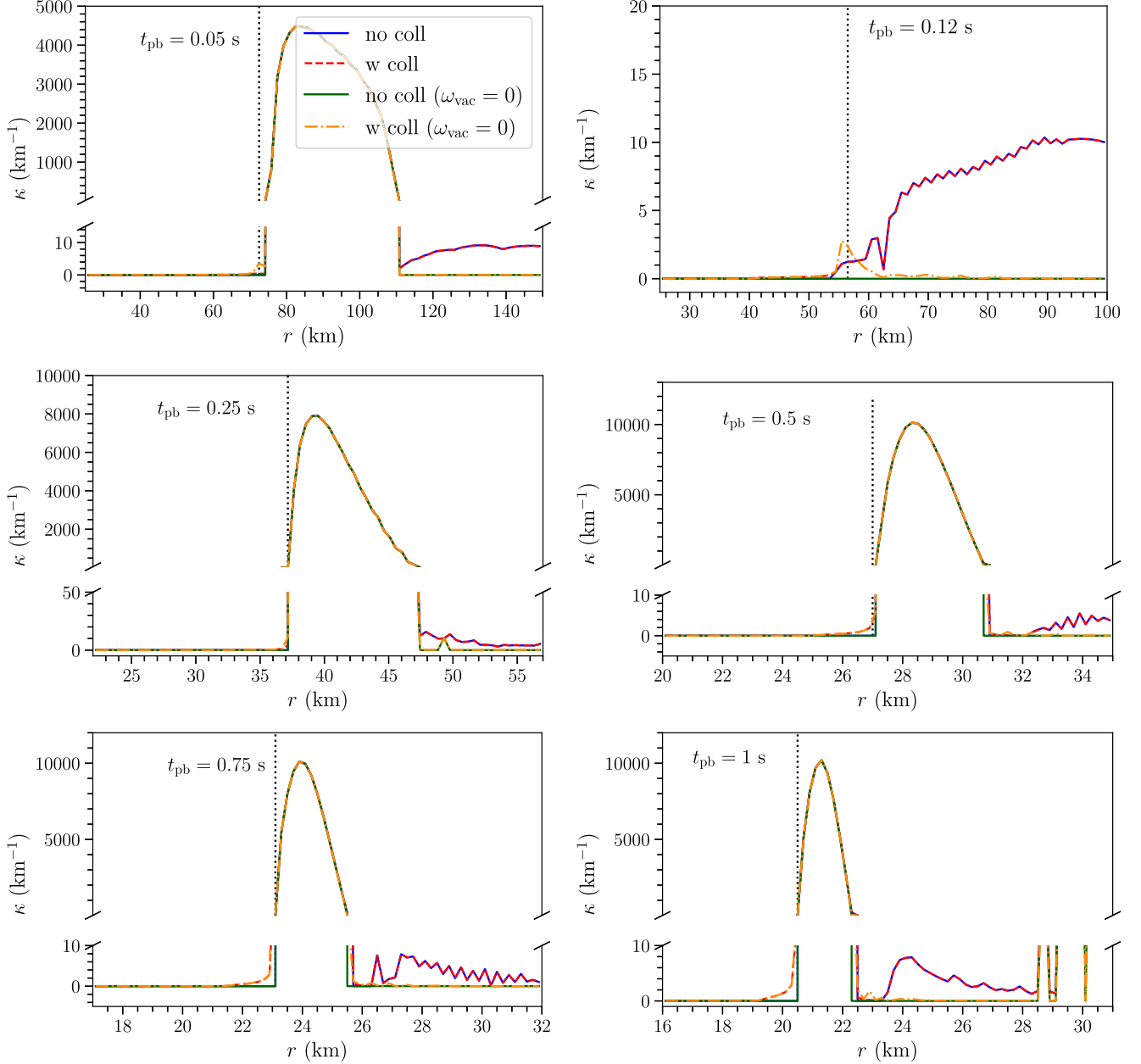


FIG. 6. Radial profile of the growth rate of the flavor instability, obtained under the assumption of homogeneity, at various time snapshots (from  $t_{\text{pb}} = 0.05$  s in the top left panel to  $t_{\text{pb}} = 1$  s in the bottom right panel). Each panel displays results obtained for four different scenarios. The blue line uses the vacuum and the self-interaction Hamiltonian (slow instability), while the green line considers only the self-interaction Hamiltonian (fast instability); for both blue and green lines, collisional damping is ignored. The same calculation is repeated to obtain the dashed red and dot-dashed orange lines, but with collisional damping. It should be noted that, except for  $t_{\text{pb}} = 0.12$  s, the four lines are almost on top of each other and difficult to distinguish. The location of the onset of ELN crossings is marked through the black vertical line to guide the eye.

$$\begin{aligned}
i \frac{\partial \rho_{ex}}{\partial t} &= [(H_{ee} - H_{xx})\rho_{ex} - (\rho_{ee} - \rho_{xx})H_{ex}] \\
&\quad - \frac{i}{2}(C_{\text{absorb}}^e + C_{\text{absorb}}^x)\rho_{ex} - \frac{i}{4}(C_{\text{dir-ch}}^e + C_{\text{dir-ch}}^x) \\
&\quad \times \int [\rho_{ex}(\cos \theta) - \rho_{ex}(\cos \theta')] d \cos \theta', \quad (10)
\end{aligned}$$

$$\begin{aligned}
i \frac{\partial \bar{\rho}_{ex}}{\partial t} &= [(\bar{H}_{ee} - \bar{H}_{xx})\bar{\rho}_{ex} - (\bar{\rho}_{ee} - \bar{\rho}_{xx})\bar{H}_{ex}] \\
&\quad - \frac{i}{2}(\bar{C}_{\text{absorb}}^e + \bar{C}_{\text{absorb}}^x)\bar{\rho}_{ex} - \frac{i}{4}(\bar{C}_{\text{dir-ch}}^e + \bar{C}_{\text{dir-ch}}^x) \\
&\quad \times \int [\bar{\rho}_{ex}(\cos \theta) - \bar{\rho}_{ex}(\cos \theta')] d \cos \theta'. \quad (11)
\end{aligned}$$

It should be noted that, due to the direction-changing contribution in the collision term, the linearized equations for  $\rho_{ex}(r, \cos \theta)$  and  $\bar{\rho}_{ex}(r, \cos \theta)$  depend on the density matrix at all other angles, due to the integral in the last term of Eqs. (10) and (11).

Equations (10) and (11) form an eigensystem for which we calculate the eigenvalues following the procedure described in Ref. [44]. In the absence of the collision term, the eigenvalues of the system are complex conjugate pairs; however, due to the presence of the collision term, this is no longer true for Eqs. (10) and (11). The eigenmode that has the eigenvalue with the largest positive imaginary term, which we denote by  $\kappa$ , dominates and is responsible for an instability for which we can compute its growth rate.

The growth rate of fast, slow, and collisional flavor instabilities is linked to three timescales of our system,  $\mu^{-1}$ ,  $\omega_{\text{vac}}^{-1}$ , and the time between two successive collisions of neutrinos—see also Refs. [13,14]. The timescale associated with the growth rate is determined by the fastest timescale that contributes to the flavor instability.

Figure 6 shows the growth rates for the fast instability [obtained by calculating the eigenvalues of Eqs. (10) and (11) when  $\omega_{\text{vac}} = 0$ , green curve], along with the growth rates obtained when the vacuum and the collision terms are included. We find regions of flavor instability for all time snapshots considered in this work. Interestingly, in all cases except for  $t_{\text{pb}} = 0.12$  s, the largest growth rate is triggered by the ELN crossing (green curve), with regions (especially at larger radii) where instabilities due to  $\omega_{\text{vac}} \neq 0$  dominate (blue and dashed red curves), but with a growth rate which is about 3 orders of magnitude smaller than the first peak. The behavior of the growth rate for  $t_{\text{pb}} = 0.12$  s represents a special case (top right panel in Fig. 6); in fact, the fast instability is absent (green line) in spite of the presence of an ELN crossing. It is the interplay between the vacuum frequency with the ELN crossing that makes the system unstable and leads to the growth rate of the blue curve. This is confirmed by the smaller (slow) growth rate that we observe in this case with respect to all other snapshots. The fact that the blue and red curves are exactly on top of each

other implies a subleading role of the collisional instability at  $r \gtrsim 56$  km. The effect of the collisional instability is visible for  $\omega_{\text{vac}} = 0$  (dot-dashed orange curve).

We conclude that the growth rate does not seem to be dominated by collisional effects (dot-dashed orange curve) across the investigated radial range and for all times, except for a few minor exceptions. In very small regions just prior to the growth of  $\kappa$  of the fast flavor instability, the collisional instability is found, albeit with a very small

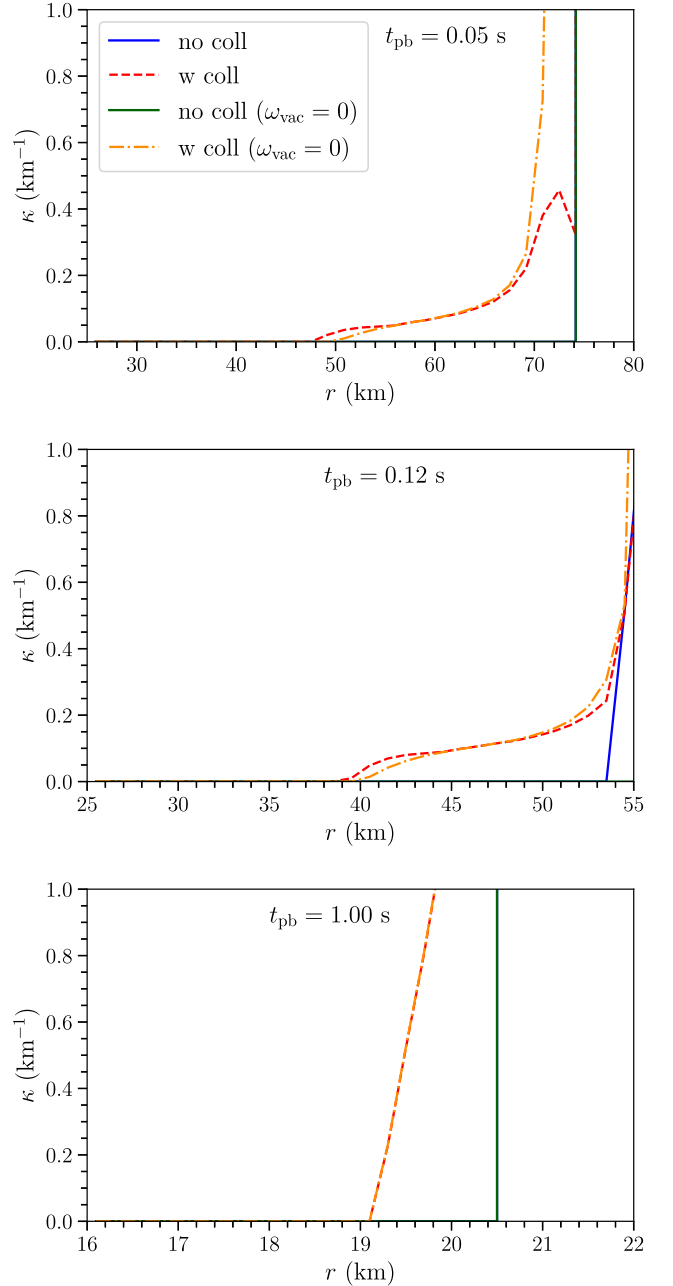


FIG. 7. Enlarged version of Fig. 6 for  $t_{\text{pb}} = 0.05, 0.12,$  and  $1$  s to highlight the radial region where the collisional instability starts to be present. In the top and the bottom panels, the blue line is not visible, as it is behind the green line.

growth rate compared to the fast flavor instability, the collisional instability having the effect of pushing the occurrence of the flavor instability to a smaller radius by a few kilometers. Hence, collisions seem to modify the effective vacuum frequency, in agreement with the findings of Ref. [32]. In order to better inspect the growth of the collisional instability, Fig. 7 shows an enlarged version of Fig. 6 for  $t_{\text{pb}} = 0.05, 0.12,$  and  $1$  s. We can clearly see a small collisional growth rate that appears just prior to the fast or slow instability; however, the impact of this small instability is likely to be negligible. The reason for this is that the flavor instability develops before neutrinos are completely decoupled from matter and, hence, forward peaked. The flavor evolution at larger radii can, thus, be transported to smaller radii because of neutrino advection; hence, the fast or slow flavor instability might still have a larger impact than collisional instability on the flavor evolution at smaller radii. These findings suggest that, if the growth rate of slow and fast instabilities should always be larger than the collisional one, then the only scenario where the collisional instability might be important should be when both fast and slow flavor instability are absent.

It should be emphasized that the presence of a flavor instability in a limited radial range does not imply that significant flavor conversion develops in or is restricted to that region; in fact, the advective term can cause the flavor content at other radii to be modified because of flavor conversion, even if the flavor instability is not initially present in a certain spatial range [13,14,47–49].

## V. IMPACT OF INHOMOGENEITY ON THE DEVELOPMENT OF THE FLAVOR INSTABILITY

In this section, we address the effect of inhomogeneities on the results presented in Sec. IV. To this purpose, we generalize Eqs. (10) and (11) to include the spatial dependence as follows:

$$i \frac{\partial \rho_{ex}}{\partial t} = -i \vec{v} \cdot \vec{\nabla} \rho_{ex} + [(H_{ee} - H_{xx})\rho_{ex} - (\rho_{ee} - \rho_{xx})H_{ex}] - \frac{i}{2} (C_{\text{absorb}}^e + C_{\text{absorb}}^x)\rho_{ex} - \frac{i}{4} (C_{\text{dir-ch}}^e + C_{\text{dir-ch}}^x) \times \int (\rho_{ex}(\cos \theta) - \rho_{ex}(\cos \theta')) d \cos \theta', \quad (12)$$

$$i \frac{\partial \bar{\rho}_{ex}}{\partial t} = -i \vec{v} \cdot \vec{\nabla} \bar{\rho}_{ex} + [(\bar{H}_{ee} - \bar{H}_{xx})\bar{\rho}_{ex} - (\bar{\rho}_{ee} - \bar{\rho}_{xx})\bar{H}_{ex}] - \frac{i}{2} (\bar{C}_{\text{absorb}}^e + \bar{C}_{\text{absorb}}^x)\bar{\rho}_{ex} - \frac{i}{4} (\bar{C}_{\text{dir-ch}}^e + \bar{C}_{\text{dir-ch}}^x) \times \int (\bar{\rho}_{ex}(\cos \theta) - \bar{\rho}_{ex}(\cos \theta')) d \cos \theta'. \quad (13)$$

It can be seen that the growth rate of  $\rho_{ex}$  and  $\bar{\rho}_{ex}$  as a function of time at a given spatial location can be modified by the spatial derivative only if  $\vec{\nabla} \rho_{ex}$  and  $\vec{\nabla} \bar{\rho}_{ex}$  are

significant in comparison to the other terms entering the kinetic equations.

If periodic boundaries are assumed, in order to perform the linear stability analysis for the inhomogeneous modes, the ansatz that  $\rho_{ex}$  and  $\bar{\rho}_{ex}$  can be represented as a combination of Fourier modes, i.e.,  $\rho_{ex}(\vec{x}) = \sum_{\vec{k}} e^{i\vec{k} \cdot \vec{x}} \tilde{\rho}_{ex}^{\vec{k}}$  and  $\bar{\rho}_{ex}(\vec{x}) = \sum_{\vec{k}} e^{i\vec{k} \cdot \vec{x}} \tilde{\bar{\rho}}_{ex}^{\vec{k}}$ , has been usually considered in the literature [50,51]. Here,  $\tilde{\rho}_{ex}^{\vec{k}}$  and  $\tilde{\bar{\rho}}_{ex}^{\vec{k}}$  are the Fourier components of the off-diagonal components of the density matrices. Plugging the expressions for  $\rho_{ex}(\vec{x})$  and  $\bar{\rho}_{ex}(\vec{x})$  in Eqs. (12) and (13), one can see that the linearized equations decouple for each Fourier mode, if and only if the Hamiltonian is independent of the spatial location, i.e.,  $\rho_{ee}$  and  $\bar{\rho}_{ee}$  are not functions of  $\vec{x}$ . If the Hamiltonian has nontrivial spatial dependence, as in our case or the one investigated in Ref. [30], this standard approach cannot be applied to investigate the growth of the inhomogeneous modes.<sup>2</sup>

To perform the linear stability analysis in the presence of inhomogeneous modes, we should seek the eigenvalues of Eqs. (12) and (13) for all spatial points simultaneously. Since this task is challenging, we look for the eigenvalues through an iterative procedure. We begin with the ansatz of collective evolution:

$$\rho_{ex}(\vec{x}) \sim Q_{\theta}(r) e^{-i\Omega(r)t}, \quad (14)$$

$$\bar{\rho}_{ex}(\vec{x}) \sim \bar{Q}_{\theta}(r) e^{-i\Omega(r)t}. \quad (15)$$

Our goal is to find the functions  $\Omega(r)$ ,  $Q_{\theta}(r)$ , and  $\bar{Q}_{\theta}(r)$  that satisfy Eqs. (12) and (13). We find the zeroth-order approximation for these functions, ignoring the advective term; note that  $\Omega^0(r)$ ,  $Q_{\theta}^0(r)$ , and  $\bar{Q}_{\theta}^0(r)$  are independent of the spatial derivative in the zeroth-order approximation. For each given location, the zeroth-order estimate of  $\Omega(r)$  denoted by  $\Omega^0(r)$  is obtained, requiring that

$$\begin{vmatrix} I[1] - 1 & -I[\cos \theta] \\ I[\cos \theta] & -I[\cos^2 \theta] - 1 \end{vmatrix} = 0, \quad (16)$$

where

$$I[f] = \int d \cos \theta \frac{\rho_{ee} - \bar{\rho}_{ee}}{\Omega^0 - H_{ee}}. \quad (17)$$

Once the eigenvalue is known, the zeroth-order estimate of the eigenvectors  $Q_{\theta}^0(r)$  and  $\bar{Q}_{\theta}^0(r)$  can be computed. With the knowledge of the approximate dependence of  $Q_{\theta}(r)$

<sup>2</sup>Note that the method adopted in the original papers proposing the linear stability analysis for the inhomogeneous modes was justified, since their goal was to explore the spontaneous breaking of spherical symmetry, without inhomogeneity in the radial direction [50,51].

and  $\bar{Q}_\theta(r)$  on  $\cos\theta$  and  $r$ , it is possible to estimate the magnitude of the advective term in Eqs. (12) and (13). This helps us to obtain an iterative estimate of the growth rate solving Eq. (16) but with the denominator that is modified to include the advective term from the previous iteration.

The advective term applied to Eqs. (14) and (15) gives

$$\vec{v} \cdot \nabla \rho_{ex} = \left( \frac{1}{Q_\theta(r)} \vec{v} \cdot \nabla Q_\theta(r) - i \frac{d\Omega(r)}{dr} \right) \rho_{ex}, \quad (18)$$

and an analogous expression holds for antineutrinos. The first term in the parentheses is generally small compared to the second term but depends on  $\cos\theta$ . The effect of the advective term is to replace  $\Omega^0$  in Eq. (17) with  $(\Omega^0 - id\Omega/dr)$ . The real part of  $d\Omega/dr$  is equivalent to adding a matter term that does not affect the growth rate of the instability. The imaginary part of  $d\Omega/dr$  shifts the imaginary part of the eigenvalue. This correction is not significant if the derivative is small compared to  $\text{Im}(\Omega^0)$ . For all the cases, we find that the results of this iterative approach lead to results that are comparable to the ones shown in Fig. 6 and, hence, are not shown.

The impact of inhomogeneities on the growth rate can also be explored solving the neutrino quantum kinetic equations numerically in the linear regime and comparing the latter with the growth rate resulting from the linear stability analysis carried out considering the homogeneous mode. Figure 8 shows such a comparison at  $r = 21.3$  km for  $t_{pb} = 1$  s. We can see good agreement. We have carried out this comparison for all snapshots and a range of radii for each time snapshot. To this purpose, however, we have used a self-interaction strength 3 orders of magnitude smaller

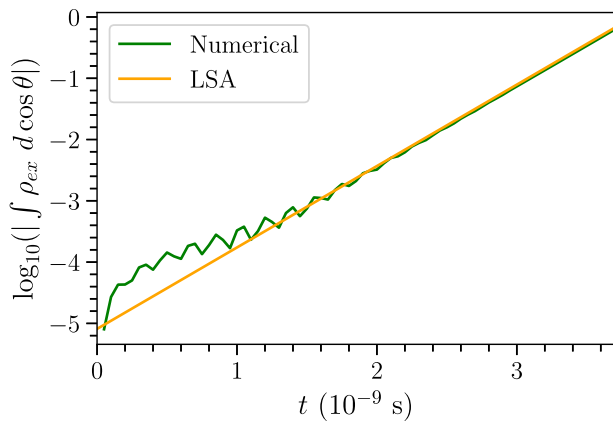


FIG. 8. Growth of  $|\int \rho_{ex} d \cos \theta|$  as a function of time at  $r = 21.3$  km for  $t_{pb} = 1$  s. The growth rate is given by the slope of  $|\int \rho_{ex} d \cos \theta|$ . The green line has been obtained by solving the quantum kinetic equations, focusing on the linear regime. The orange line shows the growth predicted by the linear stability analysis for the homogeneous mode. The excellent agreement between these two independent approaches in the linear regime suggests that the inhomogeneous modes might negligibly affect the growth rate.

than the one computed relying on the neutrino properties. The attenuation of the self-interaction strength has been employed because of the technical challenges due to the fact that the numerical simulation has to be performed for a very long time to see the exponential growth for the very small growth rates typical of certain radii. In all cases, we find good agreement between the numerical solution of the quantum kinetic equations and the linear stability analysis carried out for the homogeneous mode (results not shown here as comparable to the ones reported in Fig. 8). We note that we also find good agreement between the results of the linear stability analysis carried out considering the homogeneous mode (cf. the red dashed line in Fig. 6) and the solution of the neutrino quantum kinetic equations for  $t_{pb} = 0.12$  s. As shown in Fig. 6, for this snapshot fast instabilities are irrelevant for the homogeneous mode despite the existence of ELN crossings (cf. green line); because of the interplay between  $\omega_{vac} \neq 0$  and the ELN crossing, the system becomes unstable, with a growth rate represented by the blue curve. We note that the employment of the attenuated self-interaction strength may overestimate the relevance of the vacuum term; nevertheless, our main conclusions would not be qualitatively affected.

Our findings seem to suggest that, in the absence of periodic boundary conditions, there may be a unique growth rate that is of relevance, and it is given by the solution of Eqs. (12) and (13). This is different from what is considered in Ref. [30], when the growth rate is calculated for several Fourier modes; in this case, each Fourier mode has its own growth rate, the largest of which is interpreted as the physically relevant one. However, such an analysis assumes self-sustaining perturbations at all possible length scales, which is possible only if periodic boundary conditions are imposed. While our findings should be taken with caution due to the approximations involved, they call for dedicated work to assess the interplay of inhomogeneities with fast and collisional instabilities. To this purpose, a method to carry out the linear stability analysis in the presence of inhomogeneities and in the absence of periodic boundaries should be also worked out.

## VI. DISCUSSION AND OUTLOOK

The coherent forward scattering of neutrinos onto each other is responsible for triggering flavor instabilities that could be fast (if driven by an ELN crossing for  $\omega_{vac} = 0$ ) or slow (if the neutrino vacuum frequency also plays a role). In addition, more recently, it has been advanced the possibility that also the collision of neutrinos with the background medium could be responsible for triggering flavor conversion [16,20–22,24,30–32].

References [13,14] pointed out the possible coexistence of slow and fast instabilities in the neutrino decoupling region. Because of the non-negligible collision rate, in this paper, we aim to investigate the interplay among slow, fast, and collisional instabilities in the SN core. To this purpose,

we rely on static hydrodynamic backgrounds and thermodynamic properties extracted at postbounce times between 0.05 and 1 s from a spherically symmetric hydrodynamical simulation of a SN with mass  $18.6M_{\odot}$  [33]. We compute the neutrino angular distributions in the absence of flavor conversion solving the neutrino kinetic equations in the decoupling region for an average energy mode.

We then carry out the linear stability analysis for the homogeneous mode and investigate the occurrence of slow, fast, or collisional flavor instabilities. We find that, due to the ubiquitous existence of ELN crossings, the fast flavor instability dominates virtually in all cases, except for one time snapshot ( $t_{\text{pb}} = 0.12$  s) where the slow flavor instability dominates. Under no circumstances did we find the collisional instability to be the primary contributor to the flavor instability.

Our findings are in contrast with the analysis presented in Ref. [30]. This could be due to several reasons, such as the application in Ref. [30] of the attenuation method [52] to the self-interaction potential as well as an arbitrary rescaling of the collision term for energies above 90 MeV and an implementation of the collision term that is different from ours. This approach may have led to a fictitious growth of the collisional instabilities, which should not have occurred otherwise. Note that the growth rates in Ref. [30] (cf. their Fig. 3) are strongly time dependent due to rapidly changing number densities, whereas we assume a classical steady state in which the number densities of neutrinos do not change in the linear regime.

We have ignored the effects of energy-dependent collision terms that can be important in several ways as pointed out in Ref. [24]. However, the conclusions reached in Ref. [24] cannot be directly extended to our model, since the analysis in Ref. [24] does not assume an initial classical steady state as we do. A systematic study of collisional instabilities with energy-dependent collision terms is left to future work. The role of inhomogeneities in the development of flavor instabilities, for which we present only preliminary findings in this paper, should also be subject of future dedicated work.

In conclusion, collisional instabilities remain an intriguing possibility to trigger flavor conversion; however, it is not clear whether in neutrino-dense astrophysical environments flavor instabilities due to collisions could drive and sustain flavor conversion. Further work will be needed to analyze the development of flavor instabilities in a large set of SN models, as well as neutron star merger simulations, exhibiting a wide range of thermodynamic and neutrino properties.

## ACKNOWLEDGMENTS

We thank Thomas Janka and Evan O’Connor for insightful discussions. We are also grateful to Thomas Janka, Lucas Johns, Zewei Xiong, and Meng-Ru Wu for helpful comments on our manuscript. This project has

received support from the Villum Foundation (Project No. 13164), the Danmarks Frie Forskningsfonds (Project No. 8049-00038B), and the Deutsche Forschungsgemeinschaft through Sonderforschungsbereich SFB 1258 “Neutrinos and Dark Matter in Astro- and Particle Physics” (NDM).

## APPENDIX A: COLLISIONAL TERMS

In the interior of a core-collapse SN, several processes contribute to the production, absorption, and interaction of neutrinos with matter. The most relevant ones are bremsstrahlung, pair production, beta reactions, and direction-changing processes. In this appendix, we present the implementation of these terms in the neutrino kinetic equations [see Eqs. (7) and (8)]. Our modeling of the collisional kernel was heavily inspired by the open-source neutrino transport code NuLib [53].

It should be noted that there are other thermal processes occurring in the SN interior which we ignore, namely, plasmon decay, recombination, and photoproduction, as they are subdominant [54]. In addition, we neglect the energy-changing nonelastic neutrino-electron scattering because it is subdominant, especially for the electron-type neutrinos which determine the development of the instabilities of interest to this work. We do not consider charge current interactions on muons, since our benchmark SN simulation does not include them for simplicity, despite the fact that muons could be important [55].

For calculating beta processes and direction-changing rates, we use the flavor-dependent average energy of neutrinos extracted from our benchmark hydrodynamical SN simulation and displayed in Fig. 9, whereas for thermal processes (i.e. bremsstrahlung and pair processes) we calculate the production by integrating over the energy-dependent emission rates and calculate the total absorption rate by applying Kirchoff’s law to the energy-integrated production rate.

### 1. Link between the absorption and emission rates

The absorption and emission rates are not independent in the steady state configuration but are related by Kirchoff’s law of radiation. As a consequence of Kirchoff’s law, the emission rate is such that the number density reaches a thermal distribution asymptotically in the absence of advection. Kirchoff’s law is valid not just in thermal equilibrium, but also in a steady state. Even in the low-density region where the distribution of particles is far from thermal, Kirchoff’s law can be used to relate the absorption term to the emission one [56]:

$$\mathcal{L}^{\text{int}}[\rho_{ii}] = \eta_{\nu}(1 - \rho_{ii}) - \chi_{\nu}\rho_{ii}, \quad (\text{A1})$$

where  $\chi_{\nu}$  is the absorption rate and  $\eta_{\nu}$  is the emission rate without Pauli blocking. The right-hand side of Eq. (A1) is zero in equilibrium or, equivalently,

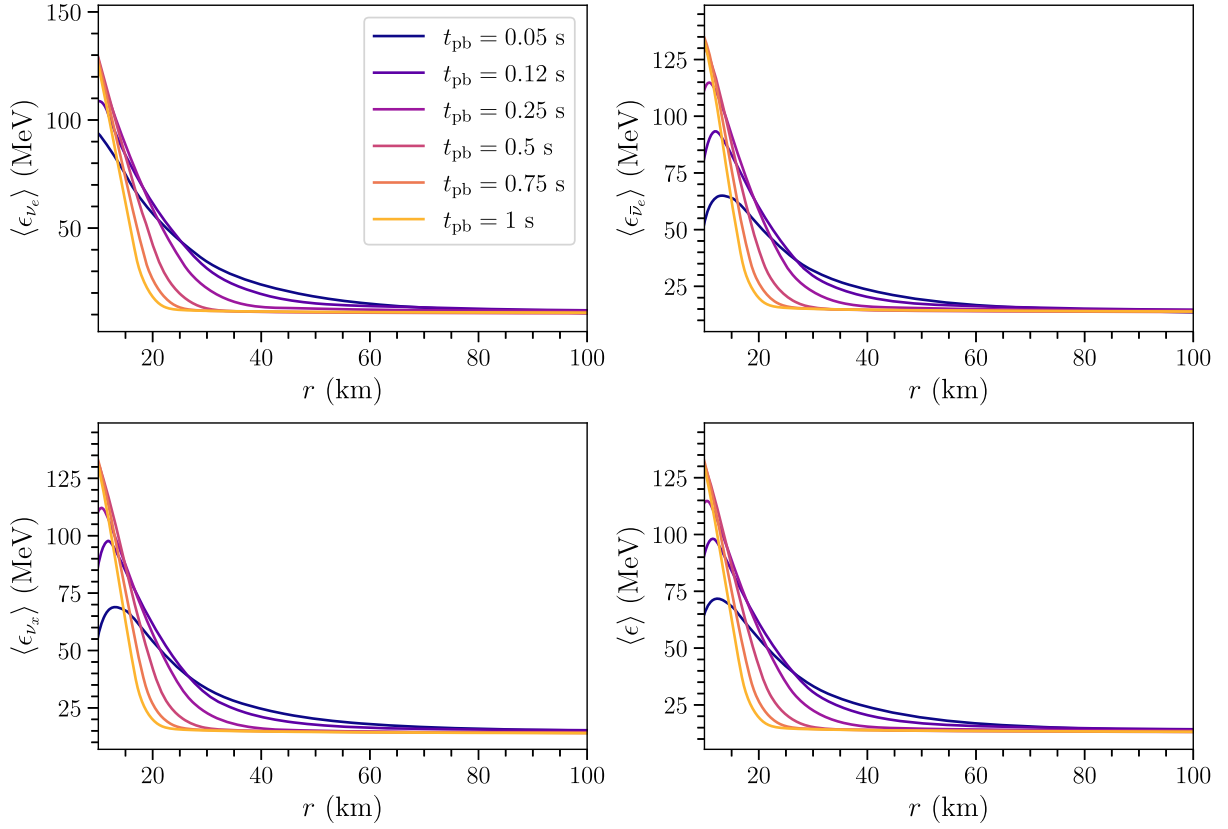


FIG. 9. Radial profile of the first energy moment for  $\nu_e$  (top left),  $\bar{\nu}_e$  (top right), and  $\nu_x$  (bottom left) for all selected postbounce times  $t_{pb} = 0.05, 0.12, 0.25, 0.5, 0.75,$  and  $1$  s extracted for our benchmark hydrodynamical SN simulation. The bottom right panel represents the flavor-averaged first energy moment that we use as characteristic neutrino energy in the linear stability analysis.

$$\eta_\nu = \chi_\nu \frac{\rho_{ii}^{\text{eq}}}{1 - \rho_{ii}^{\text{eq}}}, \quad (\text{A2})$$

with  $\rho_{ii}^{\text{eq}}$  being the Fermi-Dirac distribution of neutrinos. Substituting Eq. (A2) in Eq. (A1), we obtain

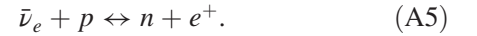
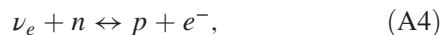
$$\mathcal{L}^{\text{int}}[\rho_{ii}] = C_{\text{absorb}}^{ii} [\rho_{ii}^{\text{eq}} - \rho_{ii}], \quad (\text{A3})$$

where  $C_{\text{absorb}}^{ii} = \chi_\nu / (1 - \rho_{ii}^{\text{eq}})$  is the absorption rate with the denominator included to account for Pauli blocking.

In the following, we discuss the emission and absorption terms. As for  $\nu_e$  and  $\bar{\nu}_e$ , charged current interactions (beta reactions) dominate over the neutral current processes, but neutral current processes are important for heavy lepton neutrinos.

## 2. Emission and absorption processes: Beta reactions

Beta reactions are the dominant channels determining the number density of electron-type neutrinos. The absorption and emission of  $\nu_e$  and  $\bar{\nu}_e$  occurs through the following interactions with free nucleons:



The correction to the beta reaction rates due to the presence of heavier nuclei is subdominant and can be neglected for our purposes.

The absorption cross section of electron neutrinos on neutrons is given by [57]

$$\sigma_{\nu_e n}^a = \sigma_0 \left( \frac{1 + 3g_A^2}{4} \right) \left( \frac{\langle \epsilon_{\nu_e} \rangle + \Delta_{np}}{m_e c^2} \right)^2 \times \left[ 1 - \left( \frac{m_e c^2}{\langle \epsilon_{\nu_e} \rangle + \Delta_{np}} \right)^2 \right]^{\frac{1}{2}} (1 - f_{e^-}) W_M. \quad (\text{A6})$$

Here,  $\sigma_0$  is the characteristic neutrino cross section,

$$\sigma_0 = \frac{4G_{\text{F}}(m_e c^2)^2}{\pi(\hbar c)^4} = 1.7612 \times 10^{-44} \text{ cm}^2, \quad (\text{A7})$$

with  $g_A = -1.254$ ,  $\Delta_{np}$  being the difference in the mass of the neutron and proton ( $m_n - m_p = 1.2933$  MeV),  $m_e$  the mass of the electron,  $\langle \epsilon_{\nu_e} \rangle$  the  $\nu_e$  average energy displayed in Fig. 9,  $f_{e^-}$  the Fermi-Dirac distribution of electrons, and

$W_M = 1 - 1.01\langle\epsilon_{\nu_e}\rangle/m_n$  the weak magnetic correction [56,58].

The related inverse transport mean free path of neutrinos is

$$\mathcal{C}_{\text{absorb}} = \sigma_{\nu_e n}^a X_n \rho_B N_A (1 - \rho_{ee}^{\text{eq}})^{-1}, \quad (\text{A8})$$

where  $\sigma_{\nu_e n}^a$  is given by Eq. (A6) and  $X_n$  and  $\rho_B$  are the neutron fraction and the baryon density shown in Fig. 2. In the expression above, we ignore the Pauli blocking of nucleons, as it is subdominant in the decoupling and free streaming region [57,59].

A similar expression holds for  $\bar{\nu}_e$  absorption with the exception that we ignore the Pauli blocking for the outgoing positron and with other appropriate changes following Ref. [57]:

$$\begin{aligned} \sigma_{\bar{\nu}_e p}^a &= \sigma_0 \left( \frac{1 + 3g_A^2}{4} \right) \left( \frac{\langle\epsilon_{\bar{\nu}_e}\rangle - \Delta_{np}}{m_e c^2} \right)^2 \\ &\times \left[ 1 - \left( \frac{m_e c^2}{\langle\epsilon_{\bar{\nu}_e}\rangle - \Delta_{np}} \right)^{27} \right]^{\frac{1}{2}} W_{\bar{M}}, \end{aligned} \quad (\text{A9})$$

with  $W_{\bar{M}} = (1 - 7.1\langle\epsilon_{\bar{\nu}_e}\rangle/m_p)$ . The inverse of the transport mean free path is defined as

$$\bar{\mathcal{C}}_{\text{absorb}} = \sigma_{\bar{\nu}_e p}^a X_p \rho_B N_A (1 - \bar{\rho}_{ee}^{\text{eq}})^{-1}. \quad (\text{A10})$$

The absorption mean free path can be used to calculate the emission rate relying on Kirchoff's law:

$$\mathcal{C}_{\text{emit}} = \mathcal{C}_{\text{absorb}} \rho_{ii}^{\text{eq}}, \quad (\text{A11})$$

$$\bar{\mathcal{C}}_{\text{emit}} = \bar{\mathcal{C}}_{\text{absorb}} \bar{\rho}_{ii}^{\text{eq}}. \quad (\text{A12})$$

It should be noted that the equality above holds for a steady state configuration and it is not necessary to have thermal equilibrium. Hence, we can use Kirchoff's law in the trapped regime, decoupling regime, and the free streaming regime. The top panels in Fig. 10 display the radial evolution of the absorption rates due to beta processes for electron neutrinos and antineutrinos for our selected postbounce snapshots.

### 3. Emission and absorption processes: Pair production

Electrons and positrons annihilate to produce pairs of neutrinos and antineutrinos:

$$e^- + e^+ \leftrightarrow \nu_i + \bar{\nu}_i, \quad i = e, x. \quad (\text{A13})$$

The  $s$ -channel Feynman diagrams can create pairs of neutrinos of all flavors, along with the  $t$ -channel diagrams that can produce only pairs of electron-type neutrinos. Note that the electron-positron pairs responsible for neutrino production are relativistic in the SN interior, and, hence, the

production cross section depends on the momenta of the initial pair.

To compute the production rate of the neutrinos, the production kernel can be decomposed in Legendre polynomials as described in Ref. [57]. Assuming that the initial electron-positron pairs are isotropically distributed, we use Eq. (C63) in Ref. [57] to calculate the production rate for all neutrino species. Note that the produced neutrinos do not have an isotropic distribution.

The emission rate can be calculated from the absorption rate. However, there are some caveats that need to be addressed. Unlike the beta processes, absorption occurs in pairs. This implies that the  $\nu_e$  absorption rate due to pair processes is overestimated in the region where there are far more  $\nu_e$ 's than  $\bar{\nu}_e$ 's. This effect is not very important for electron-type neutrinos, as the beta reaction rates dominate over the pair processes. Hence, we ignore the implications of such an approximation, but it is possible to add a correction to this overestimation of the absorption rate due to pair process [60]. The second row in Fig. 10 shows the absorption rates integrated over the neutrino energy distribution for all three neutrino flavors for different snapshots.

### 4. Emission and absorption processes: Bremsstrahlung

The reaction  $n + n \leftrightarrow n + n + \nu + \bar{\nu}$  is a subdominant thermal production process responsible for the creation of all flavors of neutrinos, and, as a consequence, it has virtually no impact on the neutrino distributions of all flavors; nevertheless, we include it in our calculations. Even in the case of heavy lepton neutrinos, the bremsstrahlung channel can be ignored in most cases, as visible from Fig. 10.

For estimating the production and absorption rates of neutrinos through bremsstrahlung, we use the following approximate formula [25]:

$$\frac{dQ'_\nu}{d\epsilon_\nu} = \frac{0.234 Q_{nb}}{T} \left( \frac{\epsilon_\nu}{T} \right)^{2.4} e^{-1.1\epsilon_\nu/T}, \quad (\text{A14})$$

$$Q_{nb} = 2.0778 \times 10^{30} \zeta X_n^2 \rho_{B,14}^2 \left( \frac{T}{\text{MeV}} \right)^{5.5}, \quad (\text{A15})$$

with  $T$  being the temperature,  $\rho_{B,14}$  the baryon density in units of  $10^{14}$  g/cm<sup>3</sup>,  $X_n$  the neutron fraction (see Fig. 2), and  $\zeta = 0.5$  the correction factor.<sup>3</sup> Equation (A15) is accurate up to 3% [56]. The emission term associated with this process is obtained by integrating the emissivity over the energy range:

<sup>3</sup>It should be noted we follow Ref. [53] and Eq. (A15) differs from Eq. (142) in Ref. [25] because of an error in that paper [61].

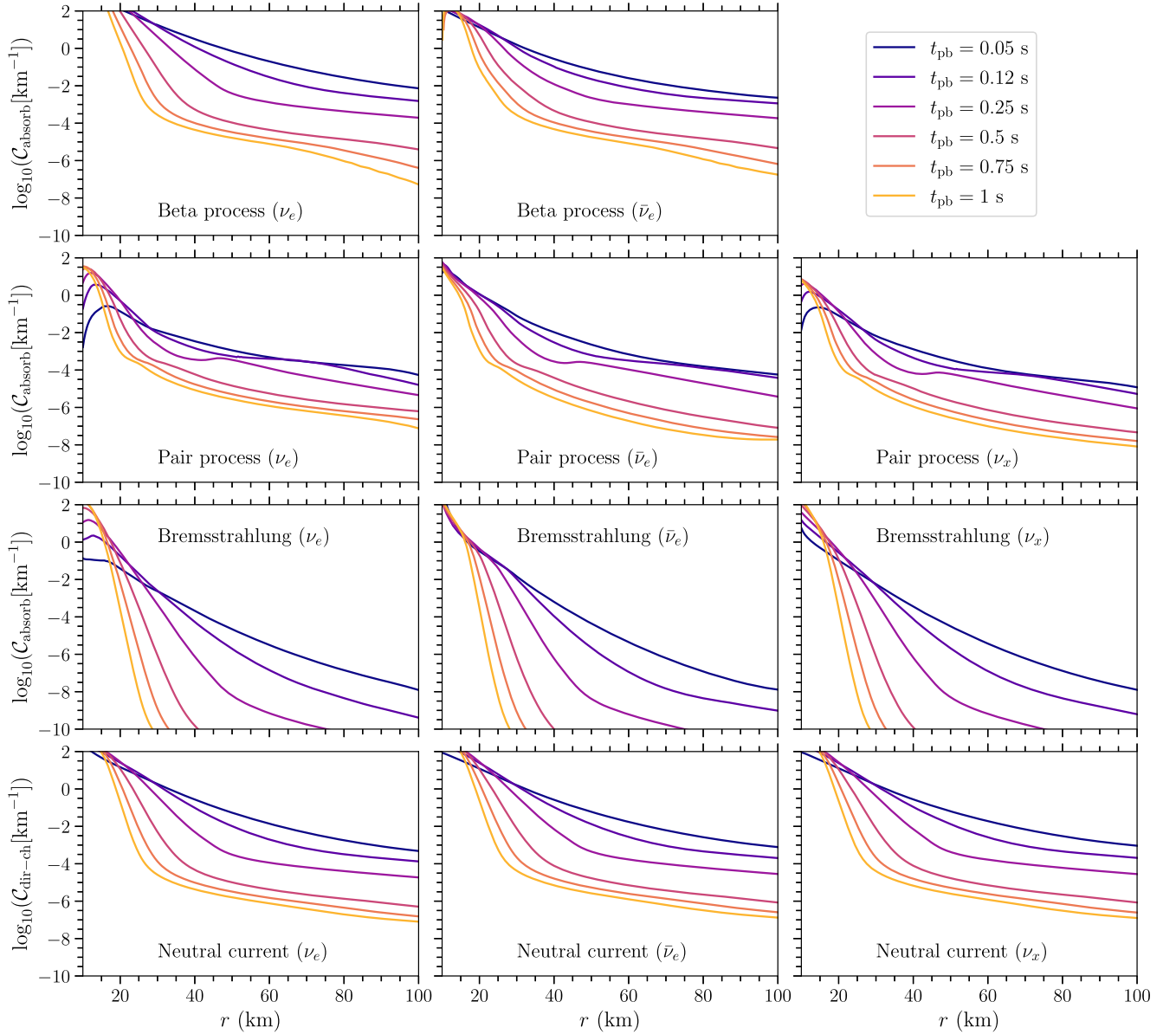


FIG. 10. Radial evolution of the absorption rates due to beta reactions for  $\nu_e$  and  $\bar{\nu}_e$  (top row; the emission rate is linked to the absorption one through Kirchoff's law), pair production (second row), bremsstrahlung (third row), and direction-changing neutral current scattering processes (bottom row) that we compute at various postbounce time snapshots and for  $\nu_e$  (left panels),  $\bar{\nu}_e$  (middle panels), and  $\nu_x$  (right panels). The difference in the interaction rate for the different flavors is due to the different average energy of each flavor. The emission rates are related to the absorption rates by Kirchoff's law. At small  $r$ , beta processes are dominant. At larger radii, direction-changing reactions start to become competitive with beta processes and are more efficient than pair and bremsstrahlung reactions, with the latter rapidly decreasing as a function of time.

$$C_{\text{emit}} = \int d\epsilon_\nu \frac{dQ'_\nu}{d\epsilon_\nu}. \quad (\text{A16})$$

The absorption term is related to the emission term through Kirchoff's law:

$$C_{\text{absorb}} = \frac{C_{\text{emit}}}{n_i^{\text{eq}}}, \quad (\text{A17})$$

which is shown in the third row in Fig. 10.

### 5. Direction-changing processes: Neutral current interactions

The momentum-changing interaction of neutrinos with matter can be due to neutral current interactions as well as charged current interactions. As for the latter, only the electron flavors ( $\nu_e$  and  $\bar{\nu}_e$ ) can participate in charged current interactions with electrons; yet, this momentum-changing process is subdominant with respect to the neutral current scattering of neutrinos with nucleons. Therefore, in the following, we focus on neutral current processes.

We calculate the momentum-changing cross section in the single-energy approximation (relying on the flavor-dependent neutrino average energy shown in Fig. 9), so the momentum-changing cross section can be viewed as a direction-changing one. The direction-changing cross section also depends on the matter composition. However, for our purposes, the contribution of nuclei (and related nuclear matrix elements) can be ignored. Hence, we focus on the interaction of neutrinos with protons and neutrons. We also ignore the neutral current interactions of neutrinos with electrons, since they are subdominant with respect to the interaction with nucleons.

As the interaction of neutrinos with nucleons is independent on the neutrino flavor, the transport cross section with neutrons and protons is given by [56]

$$\sigma_n^{\text{tr}} = \frac{\sigma_0}{4} \left( \frac{\langle \epsilon_\nu \rangle}{m_e c^2} \right)^2 \left( \frac{1 + 5g_A^2}{6} \right), \quad (\text{A18})$$

$$\sigma_p^{\text{tr}} = \frac{\sigma_0}{6} \left( \frac{\langle \epsilon_\nu \rangle}{m_e c^2} \right)^2 [(C'_V - 1)^2 + 5g_A(C'_A - 1)^2], \quad (\text{A19})$$

where  $\sigma_0$  is defined as in Eq. (A7),  $g_A = 1.254$ ,  $C'_V = 1/2 + 2 \sin^2 \theta_W$  (with  $\theta_W$  being the Weinberg angle), and  $C'_A = 1/2$ . The direction-changing collision term  $C_{\text{dir-ch}}$  as follows:

$$C_{\text{dir-ch}} = \rho_B N_A (X_n \sigma_n^{\text{tr}} + X_p \sigma_p^{\text{tr}}). \quad (\text{A20})$$

It should be noted that the direction-changing neutral current interactions are not isotropic but backward peaked. The neutrino interactions with protons have an anisotropy of about 10% ( $C_{\text{ani}} = 0.1 C_{\text{dir-ch}}$ ), whereas the interactions with neutrons have an anisotropy of about 33% ( $C_{\text{ani}} = 0.33 C_{\text{dir-ch}}$ ). This is taken into account through  $C_{\text{ani}}$ , which is the weighted average of the two anisotropies in Eqs. (7) and (8). The bottom panels in Fig. 10 illustrate the dependence of the direction-changing processes on the radius; note that the flavor dependence of the neutral current interaction rate in Fig. 10 is due to the fact that the average energy of neutrinos depends on the neutrino flavor.

## APPENDIX B: COMPARISON OF THE NEUTRINO NUMBER DENSITIES WITH THE OUTPUT OF OUR BENCHMARK SUPERNOVA MODEL

Relying on the hydrodynamical and thermodynamic quantities, local neutrino number density, and first energy moment extracted at selected postbounce times from our benchmark SN simulation, we compute the neutrino angular distributions, following the modeling of the collision term outlined in Appendix A. In this appendix, we compare the flavor-dependent and angle-integrated neutrino number densities that we obtain from postprocessing the output of our  $18.6 M_\odot$  SN model [33] with the neutrino number density extracted from the hydrodynamical

simulation to assess the degree of accuracy of our collision term. The comparison is shown in Fig. 11. Despite the good agreement between the neutrino number densities that we compute in postprocessing and the outcome of hydrodynamical simulations, we stress that the purpose of this work is not to reproduce the neutrino properties from hydrodynamical simulations but rather relies on angular distributions derived from first principles to investigate the relative importance of collisional, fast, and slow flavor instabilities.

In the SN core, neutrinos are continuously produced and absorbed at the same time (see Appendix A). These two processes eventually lead to thermal equilibration. However, the baryon density falls rapidly as a function of radius (see Fig. 2), leading neutrinos to go out of thermal equilibrium and stream freely. The radius of decoupling at which this happens depends on the magnitude of the production and absorption rates compared to the direction-changing term. As shown in Fig. 11, this implies that the neutrino number density coincides with the number density obtained by integrating Fermi-Dirac distribution over energy in the dense region, and it deviates from the energy-integrated Fermi-Dirac number density at larger radii where the matter density is lower, and the angular distribution becomes forward peaked. In order to assess the location of the neutrino decoupling surfaces in Fig. 3, we compare the local neutrino number density with the one obtained from the energy-integrated Fermi-Dirac neutrino density and define the neutrino decoupling radius as the one where the neutrino number density deviates from the Fermi-Dirac one more than 1% (see vertical lines in Fig. 11).

It should be noted that in Fig. 11 the  $\bar{\nu}_e$  number density is slightly larger than the one from the ‘‘SN model’’ because of the single-energy approximation employed in this work. We demonstrate this by performing an energy-dependent computation and report the results in Fig. 12 for the snapshot  $t_{\text{pb}} = 1$  s. The top panel in Fig. 12 shows that the discrepancy between the number densities obtained in this work and the ones from the Garching simulation is alleviated almost completely. The remaining negligible residual difference is due to the fact that our implementation of the collisional term is not identical to the one employed in the Garching simulation.

The bottom panel in Fig. 12 shows that the growth rate obtained performing a multienergy computation remains qualitatively unchanged (cf. bottom right panel in Fig. 6). It should be noted, however, that there are some quantitative differences between the single-energy and multienergy calculations: In the multienergy simulation, the maximum growth rate is slightly smaller and the region of instability is shifted to slightly larger radii. However, this does not affect our main conclusions. Figure 12, hence, demonstrates that the single-energy approximation is justified in our case.

We note that the green dotted line (i.e.,  $\bar{\nu}_e$ ) is below the red one (i.e.  $\nu_e$ ) in Fig. 11; on the other hand, the solid and red lines cross at  $\sim 22.6$  km, and the  $\bar{\nu}_e$  number density is larger than the  $\nu_e$ 's one at larger radii. Such crossing

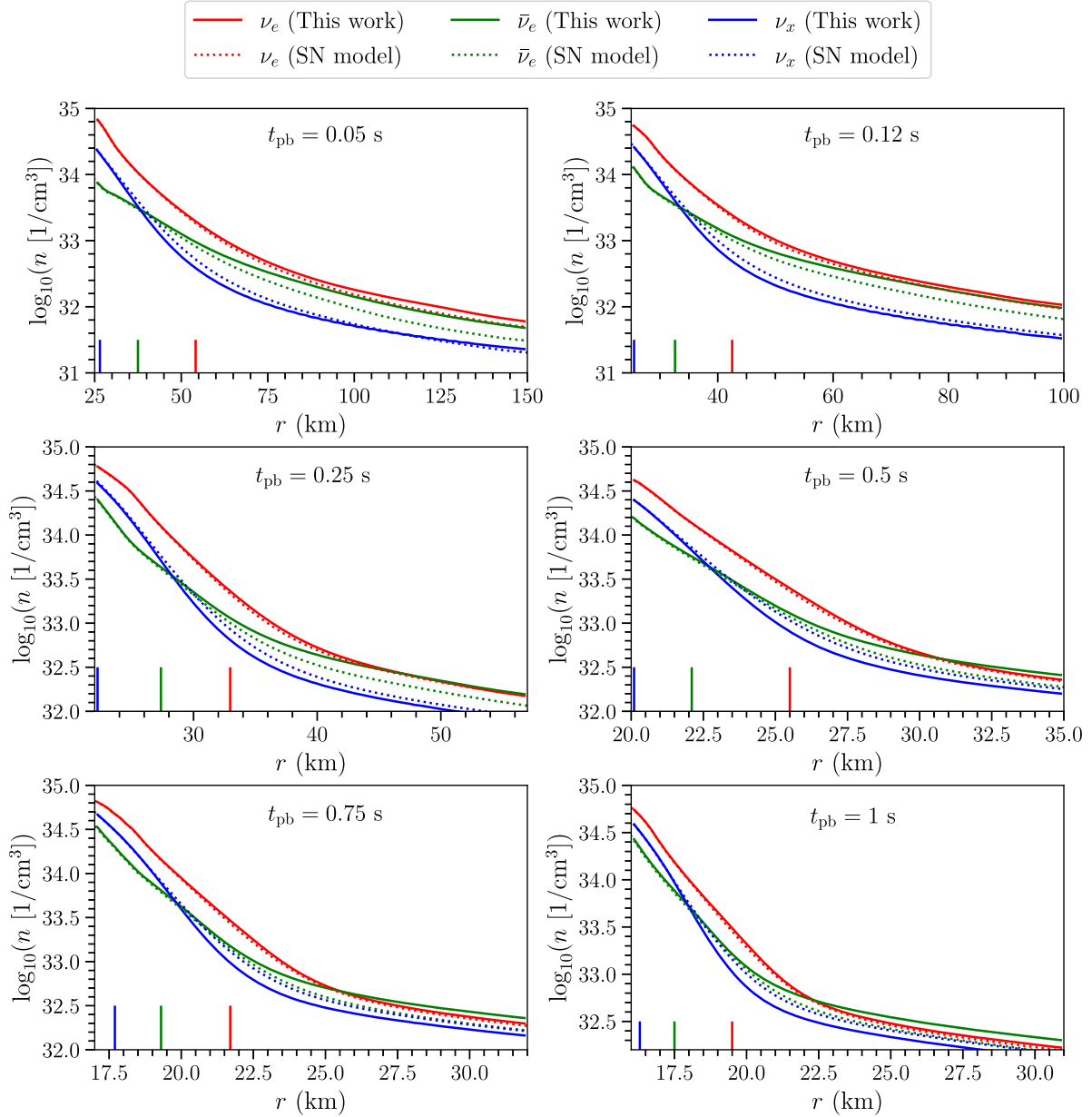


FIG. 11. Radial evolution of the neutrino number densities computed in this work (solid lines) of  $\nu_e$  (in red),  $\bar{\nu}_e$  (in green), and  $\nu_x$  (in blue) along with the ones extracted from our benchmark SN simulation (denoted by “SN model” in the legend) for selected postbounce time snapshots. The radius at which the number density of each neutrino flavor deviates from the Fermi-Dirac one corresponds to the radius of neutrino decoupling marked by a vertical line. While involving some approximations, our method allows us to reproduce the local neutrino density, which is in general agreement with the output of the hydrodynamical simulation. Note that the radial range is not the same for all time snapshots.

between the  $\nu_e$  and  $\bar{\nu}_e$  number densities is also present in our multienergy simulations in Fig. 12, although much less prominent, and it might give rise to differences in the development of ELN crossings. We conclude that the single-energy approximation slightly overestimates the number density  $\bar{\nu}_e$  facilitating the presence of a sharper ELN crossing. However, although shallower, an ELN crossing is also expected in the multienergy calculation (cf. Fig. 12). This implies that our single-energy treatment

does not affect the relative importance of fast vs collisional instabilities—the latter being dominant only in the absence of ELN crossings. In fact, a comparison between the bottom panel in Fig. 12 and the bottom right panel in Fig. 6 shows that the growth rate for fast instabilities already develops at smaller radii (the ELN crossing developing at 20.5 km for the single-energy simulation vs 21.1 km for the multienergy simulations) and is qualitatively unchanged by this feature.

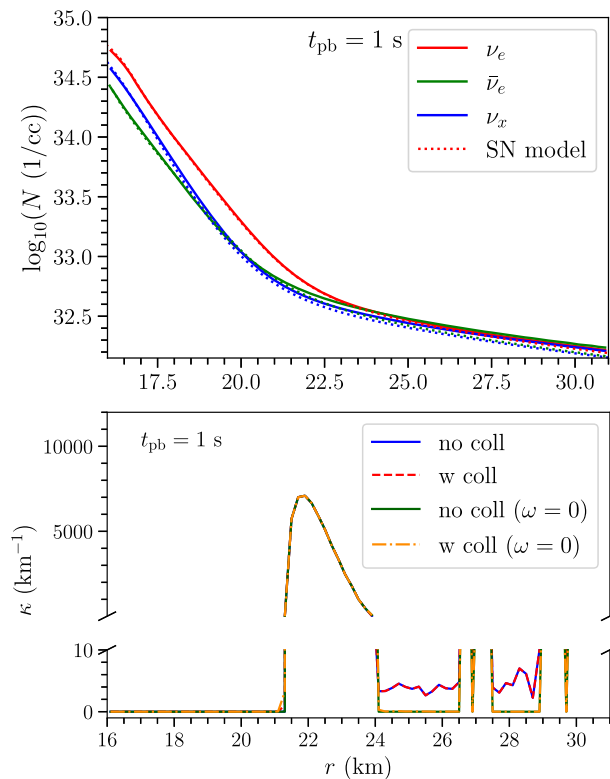


FIG. 12. Top: comparison between the neutrino number densities obtained employing multienergy dependence in the collisional rate (solid lines) and the ones coming from our benchmark SN simulation (dotted lines) for  $t_{\text{pb}} = 1$  s. The already small discrepancy between the number densities seen in Fig. 11 is further alleviated by the multienergy treatment. Bottom: growth rate of the flavor instability obtained employing multienergy dependence in the collisional rate. The qualitative feature of collisional instability not being important remains unchanged by the single-energy approximation.

- 
- [1] Alessandro Mirizzi, Irene Tamborra, Hans-Thomas Janka, Ninetta Saviano, Kate Scholberg, Robert Bollig, Lorenz HÜdepohl, and Sovan Chakraborty, Supernova neutrinos: Production, oscillations and detection, *Riv. Nuovo Cimento* **39**, 1 (2016).
- [2] Huaiyu Duan, George M. Fuller, and Yong-Zhong Qian, Collective neutrino oscillations, *Annu. Rev. Nucl. Part. Sci.* **60**, 569 (2010).
- [3] Sovan Chakraborty, Rasmus Hansen, Ignacio Izaguirre, and Georg G. Raffelt, Collective neutrino flavor conversion: Recent developments, *Nucl. Phys.* **B908**, 366 (2016).
- [4] Irene Tamborra and Shashank Shalgar, New developments in flavor evolution of a dense neutrino gas, *Annu. Rev. Nucl. Part. Sci.* **71**, 165 (2021).
- [5] Sherwood Richers and Manibrata Sen, Fast flavor transformations, *arXiv:2207.03561*.
- [6] Raymond F. Sawyer, Speed-up of neutrino transformations in a supernova environment, *Phys. Rev. D* **72**, 045003 (2005).
- [7] Raymond F. Sawyer, The multi-angle instability in dense neutrino systems, *Phys. Rev. D* **79**, 105003 (2009).
- [8] Raymond F. Sawyer, Neutrino cloud instabilities just above the neutrino sphere of a supernova, *Phys. Rev. Lett.* **116**, 081101 (2016).
- [9] Sovan Chakraborty, Rasmus Sloth Hansen, Ignacio Izaguirre, and Georg G. Raffelt, Self-induced neutrino flavor conversion without flavor mixing, *J. Cosmol. Astropart. Phys.* **03** (2016) 042.
- [10] Ignacio Izaguirre, Georg G. Raffelt, and Irene Tamborra, Fast pairwise conversion of supernova neutrinos: A dispersion-relation approach, *Phys. Rev. Lett.* **118**, 021101 (2017).
- [11] Ian Padilla-Gay, Irene Tamborra, and Georg G. Raffelt, Neutrino flavor pendulum reloaded: The case of fast pairwise conversion, *Phys. Rev. Lett.* **128**, 121102 (2022).
- [12] Taiki Morinaga, Fast neutrino flavor instability and neutrino flavor lepton number crossings, *Phys. Rev. D* **105**, L101301 (2022).

- [13] Shashank Shalgar and Irene Tamborra, Neutrino decoupling is altered by flavor conversion, *Phys. Rev. D* **108**, 043006 (2023).
- [14] Shashank Shalgar and Irene Tamborra, Neutrino flavor conversion, advection, and collisions: Toward the full solution, *Phys. Rev. D* **107**, 063025 (2023).
- [15] Shashank Shalgar and Irene Tamborra, A change of direction in pairwise neutrino conversion physics: The effect of collisions, *Phys. Rev. D* **103**, 063002 (2021).
- [16] Lucas Johns, Collisional flavor instabilities of supernova neutrinos, *Phys. Rev. Lett.* **130**, 191001 (2023).
- [17] Hirokazu Sasaki and Tomoya Takiwaki, A detailed analysis of the dynamics of fast neutrino flavor conversions with scattering effects, *Prog. Theor. Exp. Phys.* **2022**, 073E01 (2022).
- [18] Rasmus S.L. Hansen, Shashank Shalgar, and Irene Tamborra, Enhancement or damping of fast neutrino flavor conversions due to collisions, *Phys. Rev. D* **105**, 123003 (2022).
- [19] Chinami Kato and Hiroki Nagakura, Effects of energy-dependent scatterings on fast neutrino flavor conversions, *Phys. Rev. D* **106**, 123013 (2022).
- [20] Lucas Johns and Zewei Xiong, Collisional instabilities of neutrinos and their interplay with fast flavor conversion in compact objects, *Phys. Rev. D* **106**, 103029 (2022).
- [21] Ian Padilla-Gay, Irene Tamborra, and Georg G. Raffelt, Neutrino fast flavor pendulum. II. Collisional damping, *Phys. Rev. D* **106**, 103031 (2022).
- [22] Yu-Chia Lin and Huaiyu Duan, Collision-induced flavor instability in dense neutrino gases with energy-dependent scattering, *Phys. Rev. D* **107**, 083034 (2023).
- [23] Jiabao Liu, Masamichi Zaizen, and Shoichi Yamada, Systematic study of the resonancelike structure in the collisional flavor instability of neutrinos, *Phys. Rev. D* **107**, 123011 (2023).
- [24] Chinami Kato, Hiroki Nagakura, and Masamichi Zaizen, Flavor conversions with energy-dependent neutrino emission and absorption, *Phys. Rev. D* **108**, 023006 (2023).
- [25] Adam Burrows, Sanjay Reddy, and Todd A. Thompson, Neutrino opacities in nuclear matter, *Nucl. Phys.* **A777**, 356 (2006).
- [26] Hans-Thomas Janka, Explosion mechanisms of core-collapse supernovae, *Annu. Rev. Nucl. Part. Sci.* **62**, 407 (2012).
- [27] Anthony Mezzacappa, Eirik Endeve, O. E. Bronson Messer, and Stephen W. Bruenn, Physical numerical, and computational challenges of modeling neutrino transport in core-collapse supernovae, *Liv. Rev. Comput. Astrophys.* **6**, 4 (2020).
- [28] Shashank Shalgar and Irene Tamborra, On the occurrence of crossings between the angular distributions of electron neutrinos and antineutrinos in the supernova core, *Astrophys. J.* **883**, 80 (2019).
- [29] Hiroki Nagakura, Roles of fast neutrino-flavor conversion on the neutrino-heating mechanism of core-collapse supernova, *Phys. Rev. Lett.* **130**, 211401 (2023).
- [30] Zewei Xiong, Meng-Ru Wu, Gabriel Martínez-Pinedo, Tobias Fischer, Manu George, Chun-Yu Lin, and Lucas Johns, Evolution of collisional neutrino flavor instabilities in spherically symmetric supernova models, *Phys. Rev. D* **107**, 083016 (2023).
- [31] Joshua D. Martin, Joseph A. Carlson, Vincenzo Cirigliano, and Huaiyu Duan, Fast flavor oscillations in dense neutrino media with collisions, *Phys. Rev. D* **103**, 063001 (2021).
- [32] Zewei Xiong, Lucas Johns, Meng-Ru Wu, and Huaiyu Duan, Collisional flavor instability in dense neutrino gases, *Phys. Rev. D* **108**, 083002 (2023).
- [33] MPA Supernova Archive, <https://wwwmpa.mpa-garching.mpg.de/ccsnarchive/data/Bolig2016/>.
- [34] Sherwood A. Richers, Gail C. McLaughlin, James P. Kneller, and Alexey Vlasenko, Neutrino quantum kinetics in compact objects, *Phys. Rev. D* **99**, 123014 (2019).
- [35] Irene Tamborra, Lorenz Hüdepohl, Georg G. Raffelt, and Hans-Thomas Janka, Flavor-dependent neutrino angular distribution in core-collapse supernovae, *Astrophys. J.* **839**, 132 (2017).
- [36] Taiki Morinaga, Hiroki Nagakura, Chinami Kato, and Shoichi Yamada, Fast neutrino-flavor conversion in the preshock region of core-collapse supernovae, *Phys. Rev. Res.* **2**, 012046 (2020).
- [37] Sajad Abbar, Huaiyu Duan, Kohsuke Sumiyoshi, Tomoya Takiwaki, and Maria Cristina Volpe, Fast neutrino flavor conversion modes in multidimensional core-collapse supernova models: The role of the asymmetric neutrino distributions, *Phys. Rev. D* **101**, 043016 (2020).
- [38] Sajad Abbar, Huaiyu Duan, Kohsuke Sumiyoshi, Tomoya Takiwaki, and Maria Cristina Volpe, On the occurrence of fast neutrino flavor conversions in multidimensional supernova models, *Phys. Rev. D* **100**, 043004 (2019).
- [39] Milad Delfan Azari, Shoichi Yamada, Taiki Morinaga, Hiroki Nagakura, Shun Furusawa, Akira Harada, Hirotada Okawa, Wakana Iwakami, and Kohsuke Sumiyoshi, Fast collective neutrino oscillations inside the neutrino sphere in core-collapse supernovae, *Phys. Rev. D* **101**, 023018 (2020).
- [40] Hiroki Nagakura, Taiki Morinaga, Chinami Kato, and Shoichi Yamada, Fast-pairwise collective neutrino oscillations associated with asymmetric neutrino emissions in core-collapse supernovae, *Astrophys. J.* **886**, 139 (2019).
- [41] Sajad Abbar, Francesco Capozzi, Robert Glas, Hans-Thomas Janka, and Irene Tamborra, On the characteristics of fast neutrino flavor instabilities in three-dimensional core-collapse supernova models, *Phys. Rev. D* **103**, 063033 (2021).
- [42] Shashank Shalgar *et al.* (to be published).
- [43] A. Weiss, W. Hillebrandt, H. C. Thomas, and H. Ritter, *Cox and Giuli's Principles of Stellar Structure* (Cambridge Scientific Publishers Ltd., Cambridge, England, 2004).
- [44] Arka Banerjee, Amol Dighe, and Georg G. Raffelt, Linearized flavor-stability analysis of dense neutrino streams, *Phys. Rev. D* **84**, 053013 (2011).
- [45] Sagar Airen, Francesco Capozzi, Sovan Chakraborty, Basudeb Dasgupta, Georg Raffelt, and Tobias Stirner, Normal-mode analysis for collective neutrino oscillations, *J. Cosmol. Astropart. Phys.* **12** (2018) 019.
- [46] Taiki Morinaga and Shoichi Yamada, Linear stability analysis of collective neutrino oscillations without spurious modes, *Phys. Rev. D* **97**, 023024 (2018).
- [47] Shashank Shalgar, Ian Padilla-Gay, and Irene Tamborra, Neutrino propagation hinders fast pairwise flavor conversions, *J. Cosmol. Astropart. Phys.* **06** (2020) 048.

- [48] Meng-Ru Wu, Manu George, Chun-Yu Lin, and Zewei Xiong, Collective fast neutrino flavor conversions in a 1D box: Initial conditions and long-term evolution, *Phys. Rev. D* **104**, 103003 (2021).
- [49] Hiroki Nagakura and Masamichi Zaizen, Connecting small-scale to large-scale structures of fast neutrino-flavor conversion, *Phys. Rev. D* **107**, 063033 (2023).
- [50] Huaiyu Duan and Shashank Shalgar, Flavor instabilities in the neutrino line model, *Phys. Lett. B* **747**, 139 (2015).
- [51] Sajad Abbar, Huaiyu Duan, and Shashank Shalgar, Flavor instabilities in the multiangle neutrino line model, *Phys. Rev. D* **92**, 065019 (2015).
- [52] Hiroki Nagakura and Masamichi Zaizen, Time-dependent and quasisteady features of fast neutrino-flavor conversion, *Phys. Rev. Lett.* **129**, 261101 (2022).
- [53] Evan O'Connor, An open-source neutrino radiation hydrodynamics code for core-collapse supernovae, *Astrophys. J. Suppl. Ser.* **219**, 24 (2015).
- [54] Naoki Itoh, Hiroshi Hayashi, Akinori Nishikawa, and Yasuharu Kohyama, Neutrino energy loss in stellar interiors. VII. Pair, photo-, plasma, bremsstrahlung, and recombination neutrino processes, *Astrophys. J. Suppl. Ser.* **102**, 411 (1996).
- [55] Robert Bollig, Hans-Thomas Janka, Andreas Lohs, Gabriel Martinez-Pinedo, Charles J. Horowitz, and Tobias Melson, Muon creation in supernova matter facilitates neutrino-driven explosions, *Phys. Rev. Lett.* **119**, 242702 (2017).
- [56] Todd A. Thompson, Topics in the theory of core-collapse supernovae, Ph.D. thesis, The University of Arizona, 2002, <http://hdl.handle.net/10150/289816>.
- [57] Stephen W. Bruenn, Stellar core collapse: Numerical model and infall epoch, *Astrophys. J. Suppl. Ser.* **58**, 771 (1985).
- [58] Petr Vogel, Analysis of the anti-neutrino capture on protons, *Phys. Rev. D* **29**, 1918 (1984).
- [59] Georg G. Raffelt, *Stars as Laboratories for Fundamental Physics: The Astrophysics of Neutrinos, Axions, and Other Weakly Interacting Particles* (The University of Chicago Press, Chicago, 1996).
- [60] Aurore Betranhandy, Neutrino interactions and axion emission impact on core-collapse supernova simulations, Ph.D. thesis, Stockholm University, 2022.
- [61] Evan O'Connor (private communication).